Modelling electro-thermal response of lithium-ion batteries from normal to abuse conditions

Ping Ping[a], Qingsong Wang[b], Youngmann Chung[c], Jennifer Wen[a,*]

[a] Warwick FIRE, School of Engineering, University of Warwick, Library Road, Coventry CV4 7AL, UK
[b] State Key Laboratory of Fire Science, University of Science and Technology of China, Hefei 230026, China
[c] School of Engineering, University of Warwick, Library Road, Coventry CV4 7AL, UK

HIGHLIGHTS

- A 3D electro-thermal model has been developed within the frame of OpenFOAM.
- Electric conduction is coupled with heat transfer and energy balance.
- The model has been validated with published and current new experimental data.
- It captures well cell evolution from normal, abnormal cycling to thermal runaway.

ARTICLE INFO

ABSTRACT

Insight of thermal behaviour of lithium-ion batteries under various operating conditions is crucial for the development of battery management system (BMS). Although battery thermal behaviour has been studied by published models, the reported modelling normally addresses either normal operation or thermal runaway condition. A comprehensive electro-thermal model which can capture heat generation, voltage and current variation during the whole process from normal cycling to thermal runaway should be of benefit for BMS by evaluating critical factors influencing potential transition to thermal runaway and investigating the evolution process under different cooling and environment conditions. In this study, such a three-dimensional model has been developed within the frame of open source computational fluid dynamics (CFD) code OpenFOAM to study the electrical and thermal behaviour of lithium-ion batteries (LIBs). The equations governing the electric conduction are coupled with heat transfer and energy balance within the cell. Published and new laboratory data for $LiNi_{0.33}Co_{0.33}Mn_{0.33}O_2/Li_{1.33}Ti_{1.67}O_4$ (LNCMO/LTO) cells from normal cycling to thermal runaway have been used to provide input parameters as well as model validation. The model has well captured the evolution process of a cell from normal cycling to abnormal behaviour until thermal runaway and achieved reasonably good agreement with the measurements. The validated model has then been used to conduct parametric studies of this particular type of LIB by evaluating the effects of discharging current rates, airflow quantities, ambient temperatures and thickness of airflow channel on the response of the cell. Faster function losses, earlier thermal runaway and higher extreme temperatures were found when cells were discharged under higher current rates. The airflow with specific velocity was found to provide effective mitigation against over-heating when the ambient temperature was below 370 K but less effective when the ambient temperature was higher than the critical value of 425 K. The thickness of airflow channel was also found to have critical influence on the cell tolerance to elevated temperatures. These parametric studies demonstrate that the model can be used to predict potential LIB transition to thermal runaway under various conditions and aid BMS.

1. Introduction

Owing to high energy density (-400 W h L^{-1}) and long working life, lithium-ion batteries (LIBs) are widely used as the dominant power sources for portable electronic device. Their ever increasing power performance and gradually decreasing cost make them favourable for being applied in sustainable energy technologies, such as electric and hybrid electric vehicles (EV and HEVs) as well as energy storage system

Nomenclature

A	frequency factor (s^{-1})
b	Seebeck coefficient ($V\,K^{-1}$)
C_p	specific heat capacity ($J\,kg^{-1}\,K^{-1}$)
E_a	activation energy ($J\,mol^{-1}$)
a_i, b_k, E_{act}	parameters determined from experimental data by regression analysis
$f(\alpha)$	reaction model
h	convective heat transfer coefficient ($W\,m^{-2}\,K^{-1}$)
H	enthalpy ($J\,g^{-1}$)
I	current (A)
J	current density ($A\,cm^{-2}$)
k	thermal conductivity ($W\,m^{-1}\,K^{-1}$)
m	mass (g)
$n_{1,i}, n_{2,i}, n_{3,i}$	kinetic exponents for the reaction model equation
p	pressure (Pa)
Q	heat source/sink term (W)
R	gas constant ($8.314\,J\,K^{-1}\,mol^{-1}$)
S	surface area (m^2)
r	resistance of electrode (Ω)
t	time (s)
T	temperature (K)
u	velocity of the airflow ($m\,s^{-1}$)
U	equilibrium voltage (V)
V	potential of electrode (V)
α	fractional degree of conversion
Y	electrochemical conductance of the cell ($S\,cm^{-2}$)
δ	thickness (m)
ρ	density ($kg\,m^{-3}$)
σ	electrical conductivity ($S\,m^{-1}$)
κ	thermal diffusivity ($m^2\,s^{-1}$)
λ	reaction rate constant
μ	effective viscosity (Pa s)
ψ	compressibility ($s^2\,m^{-2}$)

Subscripts

c	cell
cc	current collector
con	convection
d	dynamic
e	electrolyte
ed	electrode
$elec$	electrochemical-reaction
i	various reactants for thermal reactions (i.e. n, p, sp, n_e, p_e)
n	negative electrode
p	positive electrode
rec	thermal reactions
ref	ambient
sp	separator
x, y, z	direction

in grid scale. These systems are typically of 10–100 kilowatts and megawatt or even higher scale. As such, the LIB pack in such applications typically consists of hundreds to thousands or even more LIB cells. The reliability and safety of such high density LIB packs are of critical importance. Recurrent fire incidents involving mobile phones, laptops, electric vehicles and airplanes have raised increasing concern regarding the safety of LIB during storage, transportation and utilization. LIBs may rupture, ignite or even explode when it is subjected to high-rate charging, poor ventilation, overcharging, overheating, short circuit or compression. In the above aggravating and abuse conditions, the materials within the battery react with each other, generating heat accompanied by abnormal electrical behaviour, leading to the increase of the reaction rate due to temperature rise. If the heat dissipation of the battery to the surroundings is less than the heat generation, the accumulated heat within the battery will accelerate the thermal reactions [1,2]. This causes further increase in temperature and reaction rates, and eventually thermal runaway [3,4]. Insight of the thermal properties and performance of the LIBs across various operating conditions is crucial for the development LIB management systems [4,5]. Various abuse tests have been used to investigate thermal runaway behaviour of LIBs. Effective abuse tests can directly provide information for battery thermal management. However, for various sizes and formats of LIBs and LIB packs, the development of abuse-tolerant products need numerous tests and often involve trial-and-error design processes, which are costly and time consuming [6]. As an alternative, battery electrothermal models are being developed by researchers with aims to (1) predict the performance or lifetime of LIBs and tolerance in abuse conditions and (2) predict the occurrence and consequences of thermal runaway [7]. Previous Li-ion battery models have generally focused on one of these two purposes.

The battery behaviour under normal operation has been extensively modelled. Ye et al. [8] developed an electro-thermal model to analyse the influence of ambient temperature and cycling rates on the thermal behaviour of Li-ion cell. Through different simulation conditions, the dominant heat sources for low rate and high rate discharging processes were found as reversible heat and irreversible heat, respectively. Saw

et al. [9] developed a pseudo two dimensional (2D) electrochemical mode and coupled it with lumped thermal model to study the effect of contact resistance between the cell tabs and external connectors. They found that the contact resistance caused a large temperature gradient across the cell. Liu et al. [10] simulated temperature distribution of a battery pack under different ambient temperatures, Reynolds numbers and discharge rates using a 2D transient model. The cooling effect of air, liquid and phase change material (PCM) on the battery pack were analysed and compared. The prediction indicated that the liquid coolant was generally more effective while air was better for low or sub-zero temperatures situations. The PCM was found to have maintained uniform temperature distribution on the battery pack. Khan and Kaer [11] reported a 3D model using Comsol Multiphysics™, a commercial multi-physics software, to trace the thermal gradients inside a battery pack. The model employed lumped heat source from calorimetric measurement and air cooling as heat sink. They found that higher current caused larger temperature gradient within the pack, which resulted in the requirement of sufficient inlet air velocity for better air cooling effect. Marzband et al. [12] simulated the real-time electrical behaviour of batteries under the control of an energy management system for micro grids application but they did not consider thermal behaviour. Jiang et al. [13] developed a simplified electro-thermal model which focused on cell behaviour in the low-temperature range, which was able to provide reasonable assessment of the health state of a battery in on-board battery management system (BMS). However, the heat generation for the thermal model is a lumped heat with constant active power without quantification of irreversible and reaction heat. In summary, although these published models are capable of simulating the electrical or thermal behavior of single cell or battery pack under various operation conditions, they cannot deal with thermal runaway conditions. Reactions between the battery materials which can lead to thermal runaway were not quantified in these models. In other words, the consequence of the activated thermal reactions was not predicted when the cell started to show risk of thermal runaway.

In order to simulate abuse conditions of the cell, especially thermal runaway, previous researchers have used the integration of specific

heat source in the energy balance or heat generation equation of the cell. Kim et al. [6] developed a 3D model to simulate the thermal behaviour of Li-ion cells in oven abuse tests. The thermal runaway of the cell was predicted using a lumped thermal reactions model based on the 1D thermal modeling approach similar to that proposed by Hatchard et al. [14]. By using Arrhenius formulations, the lumped model added the heat generated from thermal reactions between battery materials to the energy balance equation. Guo et al. [15] considered the reversible, irreversible and side reaction heat as the heat source in a 3D thermal model to analyse thermal runaway of the battery. The heat generation rates were obtained from experimental data rather than using kinetics evaluation. The predicted thermal runaway compared well with the oven test results. Lopez et al. [16] investigated the thermal runaway behaviour of batteries based on Arrhenius formulations of various thermal reactions reported by Kim et al. [6] and Hatchard et al. [14]. They validated the model by comparison with the oven test results. The influence of the cell configuration, electrolyte combustion and convection condition on the thermal behaviours of the battery were analysed. In all the above mentioned models, the influence of discharge and charge behaviour on the occurrence of thermal runaway was ignored. Instead, the discharge or charge process on the thermal runaway was only included in the abuse form of short-circuit, overcharge, pulse charge or discharge. Spotnitz and Franklin [17] developed a one dimension model to simulate the abuse behaviour of single cells, including overcharge, short-circuit, and nail test simulation, etc. The heat generated from overcharging and short-circuit was calculated by ohm's law from current density, conductivity and thickness of battery materials. Lee et al. [18] integrated a resistive heating process due to short-circuit current to the electrochemical and thermal behaviour of the cell. They suggested that the convective heat transfer area should be increased and the heat generation of active materials should be decreased to prevent thermal-runaway. Liang et al. [19] proposed a 3D electro-chemical-thermal model to study the thermal runaway caused by nail penetration, based on estimation of short-circuit area equivalent resistance from experimental tests. By using the commercial software Comsol Multiphysics™, Melcher et al. [20] extended a mathematical model based on the existing electrochemical model with a simple combustion model, which also followed the Arrhenius formulations. The thermal behaviour of 18,650 cells under pulse charge and discharge with 250s pulse duration has been simulated. Thermal runway under both adiabatic and convection conditions has been predicted. Although these models could predict the thermal runaway caused by

short-circuit, overcharge, pulse charge or discharge well, they are generally not applicable to cycling mode or normal operation conditions. Accidents of lithium-ion batteries have involved both operation, storage and abuse status [7,21]. External electric load under normal operation conditions may result in higher temperature of the battery which would be the potential cause of thermal runaway. The critical operation factors to influence the transition from normal cycling to thermal runaway have not been addressed and hence cannot be predicted by these previous models. Filling this knowledge gap is indeed a key objective of the present study. Such predictive capability will be of assistance to BMS and development of effective mitigation measures against thermal runaway.

The present study aims to develop and validate an electro-thermal model to predict the characteristics of a Li-ion cell from cycling to thermal runaway. The 3D electro-thermal model coupling electric conduction with heat conduction and energy balance is developed within the frame of open source computational fluid dynamics (CFD) code, OpenFOAM. The open source environment of OpenFOAM realizes the integration of electro-thermal coupled control equations for the cell and also the heat transfer between the cell and airflow. The validated model has then been applied to investigate the effect of different ambient temperatures, cycling rates and cooling conditions including velocity of airflow and thickness of the airflow channel on the onset of thermal runaway. This is followed by the study of the critical operation factors affecting the transition of a cell from normal operation to thermal runaway. The paper is organized through 5 sections with Section 1 being the Introduction; Section 2 provides details of the electro-thermal model; Section 3 introduces the experiments conducted to provide data for model validation; Section 4 reports on the model validation for both normal cycling and thermal runaway processes; Section 5 reports on the predictions of the cell characteristics under various operating conditions and discusses the effect of critical factors on the onset of thermal runaway and finally the conclusions are summarized in Section 6.

2. Details of the electro-thermal model

The cell is modelled by a solid structure formed with homogeneous layers. The effect of the environment or/and airflow cooling on the behaviour of the cell is modelled by an air structure surrounding the cell. The schematic of the 3D model is shown in Fig. 1. For numerical simulation in OpenFOAM, the finite volume discretization and variable
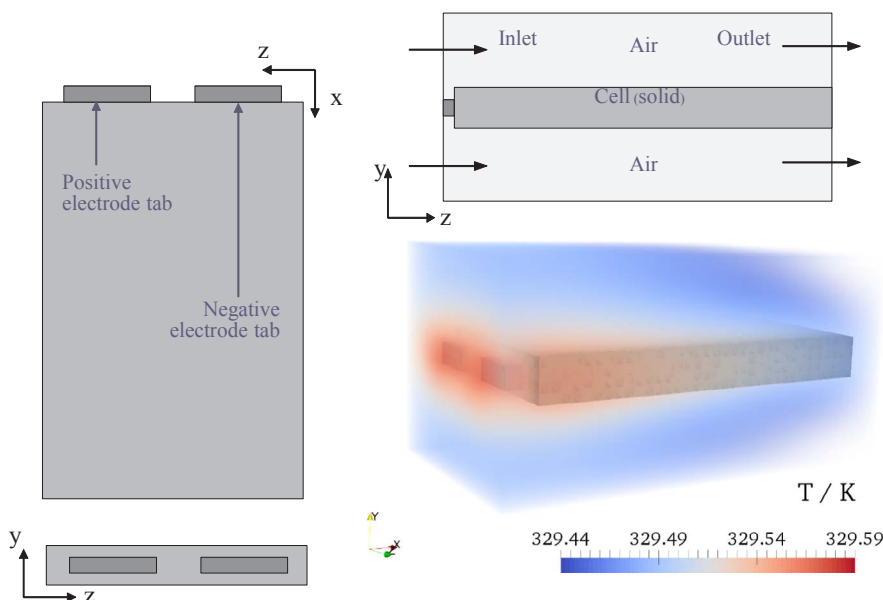

Fig. 1. Schematic of the computational model.

time step is employed. In the model, the electric conduction of the cell is treated as a time-dependent process related to the resistance, electric conductance and equilibrium voltage of the cell. The relationship between the electric conductance, equilibrium voltage and time is obtained from the experimental data. The heat generation within the cell due to irreversible and reversible electrical heating and chemical reactions are referred to as electrical heat and reaction heat, respectively. They are added as source terms in the energy equation. The convective heat transfer with the environment is computed at the boundaries to facilitate the study of various cooling effects. The heat transfer outside the cell, including the airflow, is solved from the perspective of continuity, momentum and energy equations. Table 1 lists the cell geometry, physical, thermal and electrical properties used in the present study [22–24].

The flow chart of the electro-thermal model is shown in Fig. 2. The key steps includes (1) creating the geometry and mesh, and also defining the initial conditions; (2) determining electrical parameters and thermal reaction kinetics from the experimental measurements, these are summarized in Tables 1 and 2; (3) computing the electrical heat during charge and discharge, the reaction heat from thermal reactions as well as convective heat transfer with the surroundings from the control equations given in Sections 2.2,2.3 and 2.5; and (4) iterating until the cell reaches steady-state or enters thermal runaway.

2.1. Determination of the electrical parameters

The electric properties are determined using the 2D approach developed by Kwon et al. [25], which applies Ohm's law and charge conservation on the electrodes to simulate the potential and current density distribution on the electrodes.

From the continuity of current on the electrodes and the Ohm's law, the following Poisson equations are obtained:

$$\nabla^2 V_p = -r_p J \tag{1}$$

$$\nabla^2 V_n = +r_n J \tag{2}$$

where V_p and V_n are the potential of the positive and negative electrode (V); r_p and r_n are the resistance of the positive and negative electrode (Ω); J is the current density (A cm^{-2}). The resistance r is determined by the following equation:

$$r = 1/(\delta_{cc}\sigma_{cc} + \delta_{ed}\sigma_{ed}) \tag{3}$$

where δ_{cc} and δ_{ed} are the thickness of current collector and electrode (cm); σ_{cc} and σ_{ed} are the electrical conductivity of current collector and electrode (S cm^{-1}). In view of the Seebeck effect, which is a phenomenon in which a temperature difference between two dissimilar electrical conductors or semiconductors produces a voltage difference between the two substances and effectively the conversion of heat directly into electricity at the junction of different types of wire, the polarization expression for the cell proposed by Newman [26] is modified as:

$$J = Y(V_p - V_n - U - b(T_c - T_{ref})) \tag{4}$$

where U is the equilibrium voltage (V). Y is the electrochemical conductance of the cell (S cm^{-2}). b is the Seebeck coefficient (V K^{-1}). T_c and T_{ref} are the temperature of the cell and the ambient (K). Y and U are dependent on the depth of discharge (DOD) of the cell as polynomial

functions proposed by Gu [27]. They can be determined from the experimental data using the following equations:

$$Y(\text{DOD}) = \sum_i a_i(\text{DOD})^i \exp\left[\frac{E_m}{R}\left(\frac{1}{T_{ref}} - \frac{1}{T_c}\right)\right] \tag{5}$$

$$U(\text{DOD}) = \sum_j b_j(\text{DOD})^j \tag{6}$$

where the parameters a_i, b_j, E_{act} can be obtained by using regression analysis following Chacko and Chung [28].

2.2. Electrical heat

The electrical heat generation power of the cell is evaluated from the enthalpy-of-electrochemical-reaction following the energy balance study of Bernardi et al. [29]:

$$Q_{elec} = I(U - (V_p - V_n)) - IT_c\frac{dU}{dT_c} \tag{7}$$

where Q_{elec} is the heat source of the electrochemical reaction; I is the current. The first term $I(U - (V_p - V_n))$ is indicative of the irreversible heat effect, such as the polarization heat. The difference between the equilibrium voltage U and the cell voltage $(V_p - V_n)$ is the cell overpotential, which is related with irreversibility such as ohmic losses, charge-transfer overpotentials, and mass-transfer limitations [29]. The second term $-IT_c(dU/dT_c)$ corresponds to the reversible heat effect and the entropy change [29].

2.3. Reaction heat

With the elevated temperature, abuse thermal reactions between the cell materials such as positive electrode, negative electrode and electrolyte will occur in various temperature ranges and release a great deal of heat and gas which may lead to thermal runaway of the Li-ion cell [5,17,30]. Therefore, the heat generated from the abuse thermal reactions is also evaluated quantitatively in this study. The heat is composed of several parts:

$$Q_{rec} = \sum Q_i = Q_n + Q_{n,e} + Q_{sp} + Q_p + Q_{p,e} \tag{8}$$

where Q_{rec} is the heat source of the thermal reactions; Q_i denotes the heat generation rate of one of the specific thermal reactions within the cell and can be Q_n, $Q_{n,e}$, Q_{sp}, Q_p, and $Q_{p,e}$. As reviewed by Lu et al. [5], the solid electrolyte interface (SEI) film on the surface of negative electrode decomposes firstly and generates heat at about 90–120 °C, which is Q_n in Eq. (8). Then the electrolyte reacts with the negative electrode when the temperature reaches around 120 °C [17], generating heat of $Q_{n,e}$. When the temperature reaches about 130 °C [30], the separator melts and the consecutive heat released by the short circuit is considered as Q_{sp}. Then the positive electrode decomposes partially at around 160 °C [31] with heat of Q_p. The complete decomposition of the positive electrode and the oxygen released from the positive electrode then oxidizes the electrolyte generate enormous heat, as $Q_{p,e}$.

For each thermal reaction, the heat generation Q_i can be determined by the following equation:

Table 1
Properties of cell components used in the model.

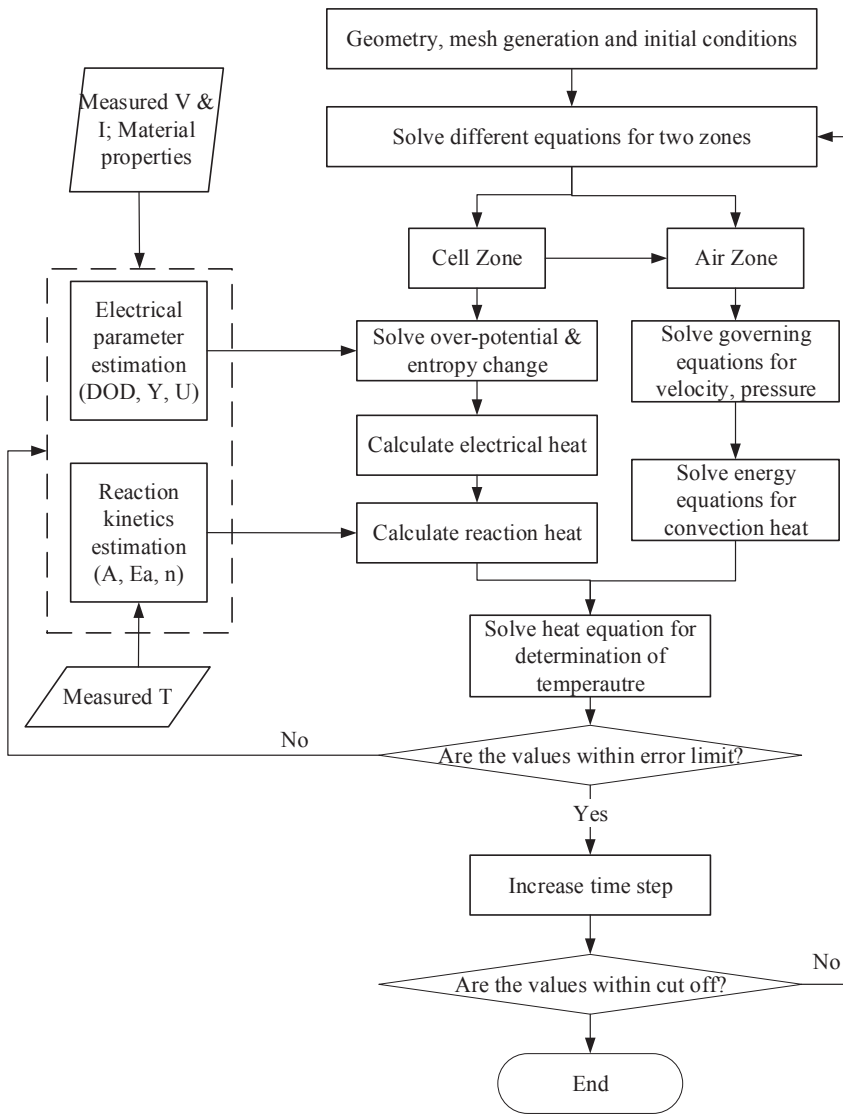|	δ (µm)	σ (s m^{-1})	k (W m^{-1} K^{-1})	C_p (J g^{-1} K^{-1})	ρ (kg m^{-3})
LNMCO electrode	56 [21]	139 [22]	5 [22]	700 [22]	1500 [22]
LTO electrode	66 [21]	100 [23]	1.04 [21]	1440 [21]	3510 [23]
Aluminum foil	100 [21]	200	238	890	2700
Separator	30	–	1 [22]	700 [22]	1200[22]
Electrolyte	–	–	–	1978 [22]	

Fig. 2. Flow chart of the electro-thermal model.

Table 2
Kinetic and thermodynamic parameters used in the model.

Stage	$T_{0,i}$ (K)	m_i (g)	H (J g^{-1})	E (kJ mol^{-1})	A (s^{-1})	$n_{1,i}$	$n_{2,i}$	$n_{3,i}$
II	353	7.5	−177.2	44.6	1.2	1[31]	0 [31]	0[31]
III	390	7.5	−383.0	220	1.1×10^{24}	1	0.3	0.2
IV	406	1.5	−110.12	205	6.5×10^{21}	1	0	0
V	429	7.35	−244.28	137	6.4×10^{12}	1 [31]	1 [31]	0 [31]
VI	479	7.35	−644.89	232	9.9×10^{17}	1	1	0.1

$$Q_i = H_i m_i \frac{\mathrm{d}\alpha_i}{\mathrm{d}t} \tag{9}$$

where H_i is the enthalpy of one of the specific thermal reactions (J g^{-1}); m_i is the mass for the specific thermal reactions (g); α_i is the fractional degree of conversion, which is related to the reaction rate constant, $\lambda(T)$ and the reaction model, $f(\alpha)$ by:

$$\frac{\mathrm{d}\alpha_i}{\mathrm{d}t} = \lambda(T)f(\alpha_i) \tag{10}$$

The following reaction model is used to describe the solid related thermal decomposition mechanisms from simple nth-order to auto-catalytic-controlled and diffusion-controlled reactions [32].

$$f(\alpha_i) = \alpha_i^{n_{i,1}}(1-\alpha_i)^{n_{i,2}}[-\ln(1-\alpha_i)]^{n_{i,3}} \tag{11}$$

By following the Arrhenius law to calculate the reaction rate constant, the following equation can be obtained:

$$\frac{\mathrm{d}\alpha_i}{\mathrm{d}t} = A_i \exp\left(-\frac{E_{a,i}}{RT}\right)\alpha_i^{n_{i,1}}(1-\alpha_i)^{n_{i,2}}[-\ln(1-\alpha_i)]^{n_{i,3}} \tag{12}$$

From Eqs. (8), (9) and (12), the heat generation rate of the abuse thermal reactions can be calculated as:

$$Q_{rec} = \sum H_i m_i A_i \exp\left(-\frac{E_{a,i}}{RT}\right)\alpha_i^{n_{i,1}}(1-\alpha_i)^{n_{i,2}}[-\ln(1-\alpha_i)]^{n_{i,3}} \tag{13}$$

The following kinetic analysis of the ARC test data is then used to obtain the parameters H_i, A_i, $E_{a,i}$ and $n_{1,i}$, $n_{2,i}$, $n_{3,i}$.

2.4. Estimation of reactions kinetics

For an adiabatic condition, the heat generated within the system will heat the system itself and there is no heat dissipation to the surroundings, the energy balance equation of the cell under adiabatic condition can be written as:

$$m_i C_{p,i} \frac{dT}{dt} = H_i m_i \frac{d\alpha_i}{dt} \tag{14}$$

where C_p is the specific heat capacity of reaction i (J kg^{-1} K^{-1}). Here, the average heat capacity of the cell $C_{p,c}$ is:

$$C_{p,c} = \frac{\sum m_i C_{p,i}}{m_c} \tag{15}$$

For the adiabatic condition, the initial and maximum temperature, T_0 and T_{max}, can then be obtained. The heat generation can be calculated as:

$$-H_i = C_{p,i}(T_{\max,i} - T_{0,i}) \tag{16}$$

The temperature rise rate can be expressed as:

$$\frac{dT}{dt} = (T_{\max,i} - T_{0,i}) A_i \exp\left(-\frac{E_{a,i}}{RT}\right) \alpha_i^{n_{1,i}} (1-\alpha_i)^{n_{2,i}} [-\ln(1-\alpha_i)]^{n_{3,i}} \tag{17}$$

By integrating over time of Eq. (14), the following equation can be obtained:

$$m_i C_{p,i}(T_i - T_0) = H_i m_i \alpha \tag{18}$$

Then the fractional degree of conversion can be determined as the following equation, by substituting Eq. (16) into Eq. (18):

$$\alpha_i = \frac{T - T_{0,i}}{T_{\max,i} - T_{0,i}} \tag{19}$$

Then Eq. (17) can be re-written as:

$$\frac{dT}{dt} = (T_{\max,i} - T_{0,i}) A_i \exp\left(-\frac{E_{a,i}}{RT} \right) \left(\frac{T - T_{0,i}}{T_{\max,i} - T_{0,i}} \right)^{n_{1,i}} \left(\frac{T_{\max,i} - T}{T_{\max,i} - T_{0,i}} \right)^{n_{2,i}} \left[-\ln\left(\frac{T_{\max,i} - T}{T_{\max,i} - T_{0,i}} \right) \right]^{n_{3,i}} \tag{20}$$

Eq. (19) can be transformed to (20) by taking logarithm:

$$\ln\left(\frac{dT/dt}{(T_{\max,i} - T_{0,i}) \left(\frac{T - T_{0,i}}{T_{\max,i} - T_{0,i}} \right)^{n_{1,i}} \left(\frac{T_{\max,i} - T}{T_{\max,i} - T_{0,i}} \right)^{n_{2,i}} \left[-\ln\left(\frac{T_{\max,i} - T}{T_{\max,i} - T_{0,i}} \right) \right]^{n_{3,i}}} \right)$$
$$= \ln A_i - \frac{E_{a,i}}{R} \cdot \frac{1}{T} \tag{21}$$

By plotting the curve of

$$\ln\left(\frac{dT/dt}{(T_{\max,i} - T_{0,i}) \left(\frac{T - T_{0,i}}{T_{\max,i} - T_{0,i}} \right)^{n_{1,i}} \left(\frac{T_{\max,i} - T}{T_{\max,i} - T_{0,i}} \right)^{n_{2,i}} \left[-\ln\left(\frac{T_{\max,i} - T}{T_{\max,i} - T_{0,i}} \right) \right]^{n_{3,i}}} \right) \text{ versus } 1/T,$$

the parameters A_i, $E_{a,i}$ can be calculated from the slope and interception of the curve as shown in Fig. 3. The T_α in Fig. 3 is the abbreviation of $(T_{\max,i} - T_{0,i}) \left(\frac{T - T_{0,i}}{T_{\max,i} - T_{0,i}} \right)^{n_{1,i}} \left(\frac{T_{\max,i} - T}{T_{\max,i} - T_{0,i}} \right)^{n_{2,i}} \left[-\ln\left(\frac{T_{\max,i} - T}{T_{\max,i} - T_{0,i}} \right) \right]^{n_{3,i}}$. The parameters $n_{1,i}$, $n_{2,i}$ and $n_{3,i}$ are selected based on a best fit of experimental data or previously reported kinetic models in [32]. All the parameters used thus determined for use in this study are summarized in Table 2.

2.5. Convective heat and fluid dynamic of the airflow

For the energy balance of the cell, the heat transfer with the surroundings is calculated by following the equation for convective heat transfer:
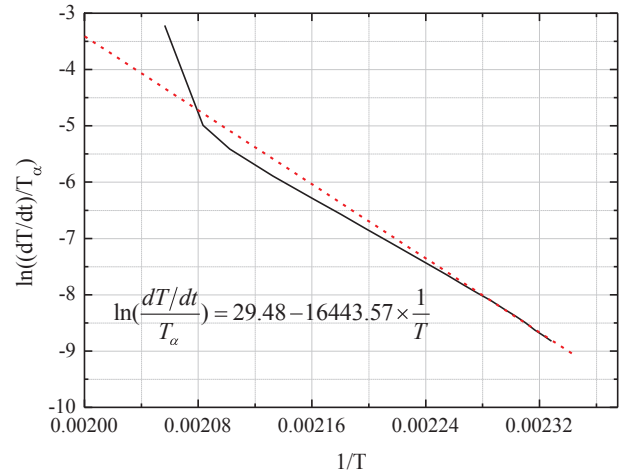

Fig. 3. The plot of $\ln((dT/dt)/T_\alpha)$ vs $1/T$ used for calculating some kinetic parameters.

$$Q_{con} = Sh(T - T_{ref}) \tag{22}$$

where, Q_{con} is heat source of the convection; S is the surface area; and h is convective heat transfer coefficient. The three-dimensional heat conduction equation within the cell can be written as:

$$\rho C_p \frac{\partial T}{\partial t} = \frac{\partial}{\partial x}\left(k_x \frac{\partial T}{\partial x}\right) + \frac{\partial}{\partial y}\left(k_y \frac{\partial T}{\partial y}\right) + \frac{\partial}{\partial z}\left(k_z \frac{\partial T}{\partial z}\right) + Q_{elec} + Q_{rec} + Q_{con} \tag{23}$$

where ρ is the density; kx, k_y and k_z are the thermal conductivity at x, y and z direction. For the airflow region, to solve the time dependent characteristics of the flow, the following governing equations are employed:

Continuity:

$$\frac{\partial \rho}{\partial t} + \nabla \cdot (\rho u) = 0 \tag{24}$$

Momentum:

$$\frac{\partial(\rho u)}{\partial t} + \nabla \cdot (\rho u \cdot u) = \nabla \cdot (\mu \nabla u) - \nabla p_d - \nabla \rho gH \tag{25}$$

Energy:

$$\frac{\partial(\rho H)}{\partial t} + \nabla \cdot (\rho u) - \nabla \cdot (\kappa \nabla H) = \frac{\partial p}{\partial t} + u \cdot \nabla p \tag{26}$$

The total pressure p is determined by:

$$p = p_d + \rho gH + p_{ref} \tag{27}$$

where u is the velocity of the air flow; μ is the effective viscosity; p is the pressure; p_d and p_{ref} are the dynamic pressure and ambient pressure; g is the gravitational acceleration.

In addition, the relation between the three components of the total pressure can be described by the following pressure correction equation:

$$\frac{\partial(\psi p_d)}{\partial t} + \frac{\partial(\psi \rho)}{\partial t} \cdot gh + \frac{\partial \psi}{\partial t} \cdot p_{ref} + \nabla(\rho u) - \Delta(\rho u) \cdot p_d = 0 \tag{28}$$

where ψ is the compressibility, which is related to the temperature:

$$\psi = \frac{1}{RT} \tag{29}$$

The equation of state for ideal gas is employed to for the air:

$$\rho = \frac{p}{RT} \tag{30}$$

2.6. Grid sensitivity analysis

Three meshes of different resolutions are defined as coarse, medium and fine mesh with 140,800, 475,200 and 1,126,400 grid points. As shown in Fig. 4a, cells at adiabatic conditions show small discrepancy on the temperature variation. Considering there is no inlet and outlet for airflows in the air part under adiabatic condition, the small discrepancy is reasonable. When airflow is present in the air part at $1\,\text{m s}^{-1}$ velocity, evident differences among the three meshes can be found as shown in Fig. 4b. The coarse mesh case shows quite different behaviour which is unphysical as the temperature keeps increasing and does not reach steady-state. In this work, the steady-state occurs when the cell is not in adiabatic condition and heat transfer happens between the cell and the surroundings. The steady-state includes two situations: (1) the cell is in a normal cycling state and in which the temperature of the cell shows periodically change; (2) the temperature of the cell shows few change with time, even the normal cycling cannot be sustained. The medium and fine mesh cases show trivial differences on both adiabatic and air cooling conditions. Therefore, the medium mesh is employed in the subsequent simulations in the present study.

3. Experiments considered

For validation of the newly developed electro-thermal model, experimental measurements of electro-thermal behaviour of prismatic Li-ion cells, which are widely used in EVs, HEVs and energy storage systems, are used. Both experimental data previously published by the authors [22] as well as new test data gathered in the present study have been used. The experimentally tested cell was composed of Li-Ni$_{0.33}$Co$_{0.33}$Mn$_{0.33}$O$_2$ (LNCMO) positive electrode and Li$_{1.33}$Ti$_{1.67}$O$_4$ (LTO) negative electrode. The electrolyte was composed of lithium salt LiPF$_6$ and carbonate solvent ethylene carbonate/diethyl carbonate/dimethyl carbonate. The size of the cell is 68 mm (L) × 36 mm (W) × 8 mm (H).

As shown in Fig. 5, the cell was put in the adiabatic chamber of ARC (THT, UK), hanging to a specially designed cell holder. The ARC is a highly adiabatic calorimeter which facilitates quantitative investigation of temperature and pressure variation of reactive mixtures. The temperature range of the ARC is 0–500 °C with heating step of 5 °C and waiting time of 15 min. The sensitivity of ARC is 0.02 °C min^{-1}. It provides effective evaluation of the thermal and safety properties of the sample. For the standard ARC test, the sample is always put in a high-pressure bomb with an attached thermal couple inside the adiabatic chamber. Given the size of the cell is larger than the bomb, the thermocouple was attached to the cell surface without using the bomb to

obtain the temperature variation during the test.

As shown in Fig. 5, the cell was cycled by a cycler (LAND CT2001-B, China) through the connection between the cell tabs and the cycler with the nickel strap. The full scale range for voltage and current test of the cycler are 25 mV to 5 V and 0.5 mA to 3 A, respectively. The accuracy of the voltage and current test is ± 0.05% of full scale. The relative deviation of the measured data is 0.05%. Before putting the tested cells into the adiabatic chamber, they were cycled outside the ARC by the cycler to verify their uniformity and reliability. The cells were firstly discharged to 2.8 V at 0.1 A, and then charged from 2.8 to 4.2 V and discharged from 4.2 V to 2.8 V using 0.05 A current for 3 cycles. The capacities of the cells are 945 mA h. Based on this capacity, the current values are 94.5, 189, 472.5, 945 and 1417.5 mA for 0.1, 0.2, 0.5, 1 and 1.5 C rate cycling, respectively.

During the ARC-LAND tests, the temperature, voltage and current variation of the cells were recorded, from which the electro-thermal behaviour of the cells could be obtained synchronously.

4. Model validation

4.1. Model validation for normal discharging and charging cycling process

The predictions for a cell discharging at various current rates under adiabatic condition are compared with experimental measurements [30]. Fig. 6 shows the average voltage and temperature variation of the cell centre during discharge from 298.2 K. The predicted discharge behaviour at various currents is in good agreement with the measurements. The offsets of the discharge plateau caused by the polarization are also well captured by the numerical simulation. The discrepancy between the predicted and test result in the case of 1.0 C rate is thought to be caused by the abnormal pulsation of the voltage during the recording of the experimental data. The predicted average temperatures are consistent with the measurements. Fig. 6(b) shows that the rate of temperature rise increases with the current rate, which can be explained by Eqs. (9) and (23). As the current increases, the heat generation and the rate of temperature rise also increases. It should be noted that the variation of temperature does not increase with the current. This is owing to the longer discharging time under lower current. Since the battery was under adiabatic condition, the generated heat was all used for self-heating, resulting in temperature rise accumulating with time. It is anticipated that in the situation of discharging under high current rate, the temperature increase will be larger than that under low current rate for the same time interval.

The predicted charge and discharge cycling behaviour is also compared with the measurements [22]. Serving as an illustration, Fig. 7
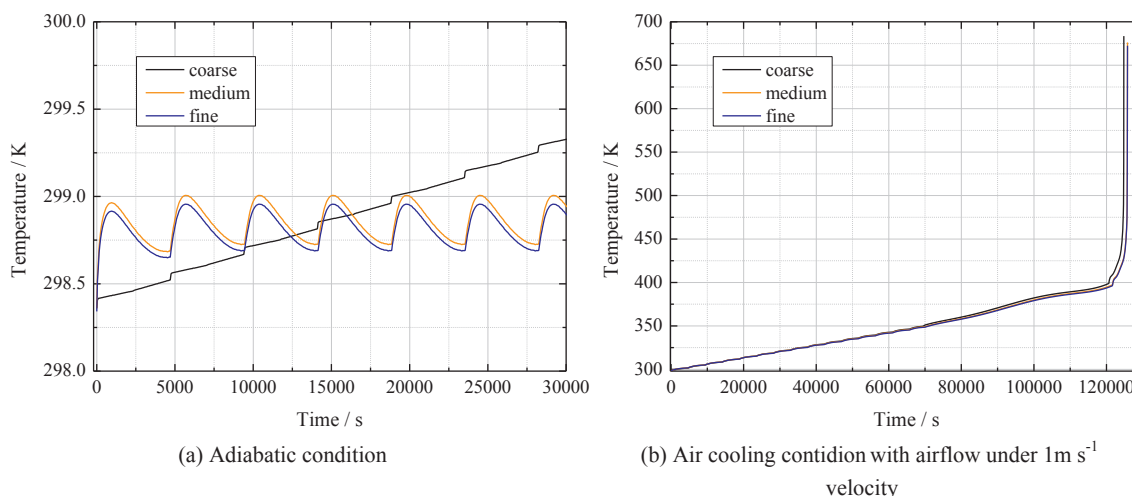

(a) Adiabatic condition   (b) Air cooling contidion with airflow under 1m s^{-1} velocity
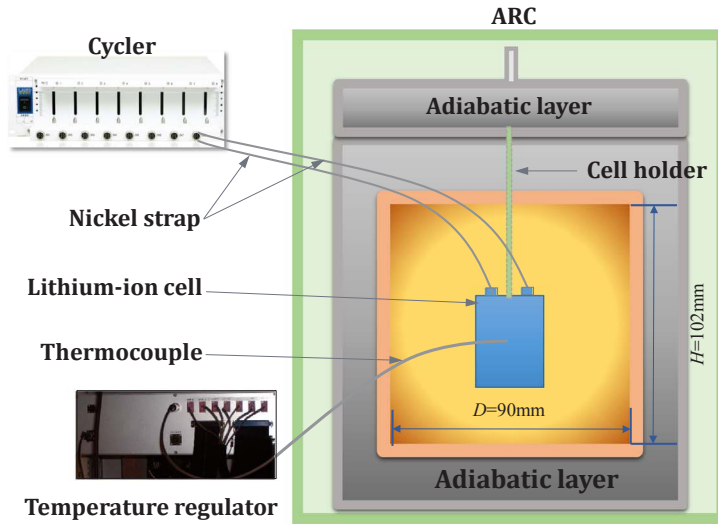
Fig. 4. Results of grid sensitivity study.

Fig. 5. Schematic of the experimental setup.

shows the average voltage, current and temperature variation during the charge and discharge process at 0.5 C rate. From Fig. 7(a) and (b), it can be seen that the predicted voltage and current are close to the measurements. The marginal deviation between the prediction and measurements are thought to be due to the different cycling time for each cycle between the predictions and the tests. In the simulation, the charge or discharge time for each cycle is dependent on the current rate and hence is constant. This is, however, not the case in the experiments due to the irreversible capacity and fading effect. Also due to the polarization, the discharge plateau in the prediction is slightly higher than that of the measurements. Fig. 7(c) shows that the predicted temperature of the cell center keep on increasing under adiabatic condition, and as expected, with a similar pattern to the measured temperature.

4.2. Model validation for thermal runaway

During self-heating in the adiabatic tests, the sustained increase of temperature will finally activate the thermal runaway of the cell. Fig. 8 shows comparison of the predicted temperature, temperature gradient and voltage with fresh measurements conducted in the present study at the current of 1.5 C under adiabatic condition. To achieve full state of charge of the cell for each cycle, the tests employed constant current mode during discharge and constant voltage mode during charge. To reproduce the electric behaviour, the normal cycling of the cell is simulated with the electrical model. The abnormal charging and

discharging behaviour of the cell are calculated from the experimental data. Because of the cell functional disorder, the discharge and charge process are fully transient with pulse current, which can be directly adopted from the experimental data. As a result of these transient processes, the voltage of the cell also fluctuated quickly as shown in Fig. 8(a). By using the pulse current taken from the experimental data as input parameters, the model has well captured the electric behaviour of the cell under adiabatic condition. Fig. 8(b) shows more details of the normal cycling process. The minor differences between the predictions and the measurements can also be accounted for by the aforementioned reason, i.e. the time for each cycle is constant in the prediction but changes in the tests. Fig. 8(c) shows the variation of the self-heating rate for the cell in the ARC test, which can be divided into several stages from stage (I) to stage (VI). For stage (I), the cell cycles in the normal way and the relative heat generated during this stage is the Q_{elec} defined in Section 2. For the following five stages, the materials within the cell begin to react with each other or by themselves and resulted in thermal runaway. Based on the definition of Q_{rec} in Section 2.3, the component heat Q_n, Q_{sp}, Q_{n_e}, Q_p and Q_{p_e} are qualified as the heat source for stage (II)-(VI), respectively. For these stages, the dynamic analysis described by Eqs. (14)–(21) is conducted to obtain the key parameters for the model and summarized in Table 2. These parameters are used as input to the electro-thermal model to predict the cell thermal behaviour.

Fig. 8(d) shows the comparison of the predicted self-heating rate of the cell with fresh measurements under adiabatic condition. It can be
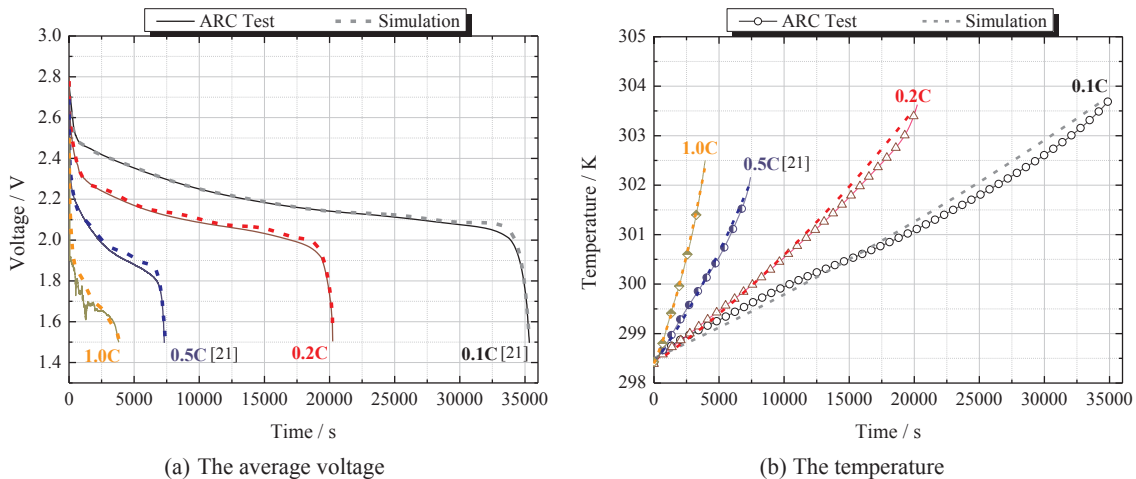

(a) The average voltage

(b) The temperature

Fig. 6. Average voltage and temperature variation of the cell centre during discharge from 298.2 K.

(a) The voltage
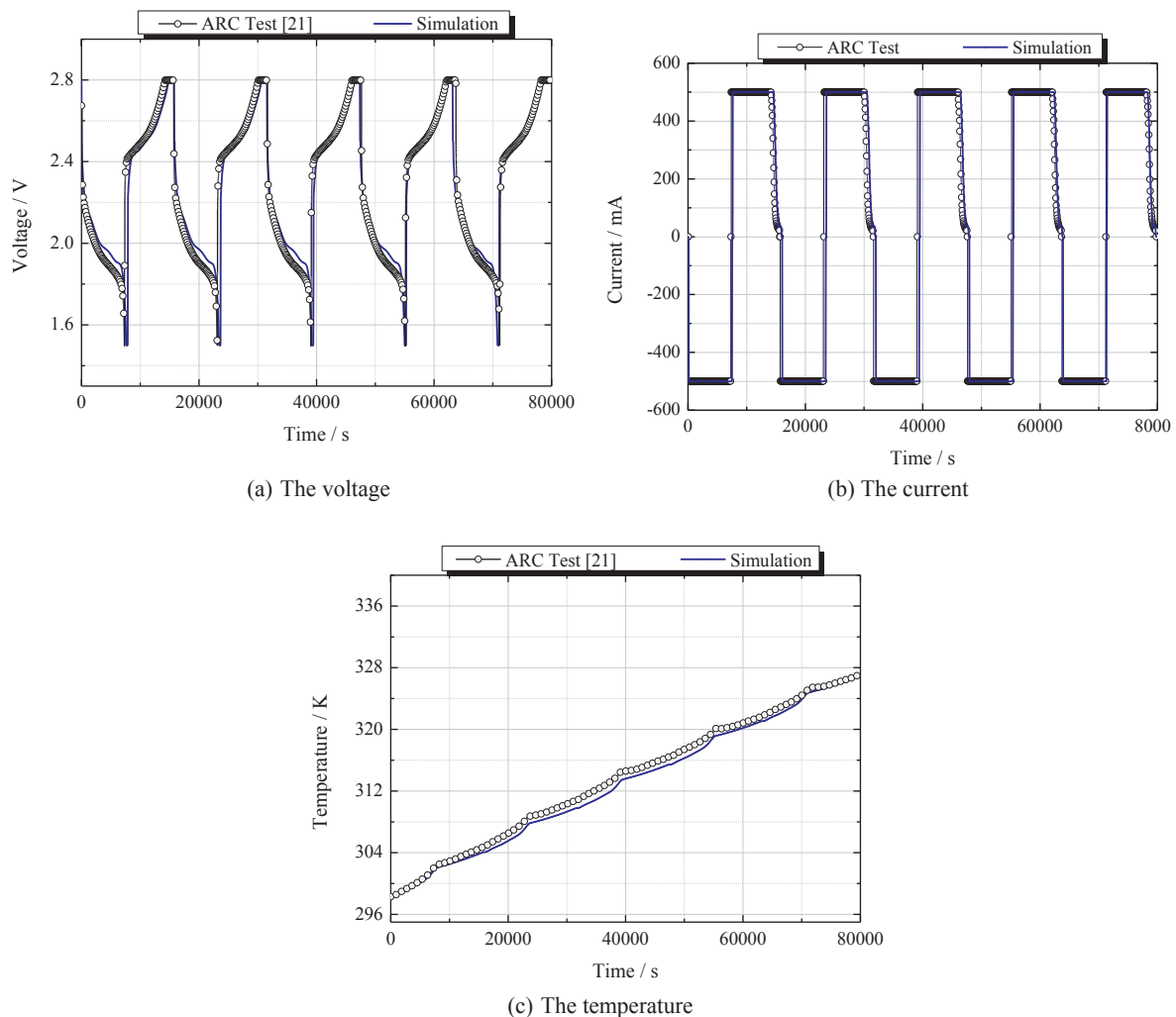

(b) The current

(c) The temperature

Fig. 7. Average voltage, current and temperature variation during the charge and discharge process at 0.5 C rate.

seen that the two curves are close for all the five different stages. The minor discrepancy between them is likely due to some error in the key parameters used for each stage. The activation energy and pre-exponential factor were found to be sensitive to the predictions. The results here demonstrate that the evolution of the cell from normal cycling to abnormal behaviour and then thermal runaway can be well captured by the present electro-thermal model. The initial warm-up of the cell during the cycling process shows a similar periodicity in terms of changes of the self-heating rate in both the predictions and experiments. The quantity, tendency and duration of the variation in the self-heating rate during the following thermal runaway process are also well captured by the predictions. For the temperature variation, one can find comparison of the predicted and measured data in Fig. 8(e) and (f) for the normal cycling mode as well as the whole process containing thermal runaway. During normal cycling, the temperature of the cell increases cyclically and continuously with the increase of the cycling number. Given that the dominant heat source of the cell is Q_{elec} during the normal charging and discharging process, the minor discrepancy between the model prediction and test data is attributed to the differences between the electric behaviour of the two cases as plotted in Fig. 8(b). Both the time and temperature for the predicted thermal runaway course are very close to the measurements although the predicted maximum temperature of 675 K reached by the cell is higher than measured peak of 615 K. This discrepancy might have been caused by two reasons. Firstly, this might be due to the ejecta event during the ARC test. When the thermal runaway occurred, the cell in the test

ruptured and spouted gas and battery materials. Large amount of heat was taken away with the ejecta. The newly developed model at its current status does not consider the ejecta event due to complexity of the variation in the pressure and heat generated within the cell during the ejecta event. To the best of our knowledge, this complexity has not been taken into account in any published thermal runaway models [15–19]. Secondly, the thermocouple, which is taped on the surface of the cell, might detect a lower temperature than the real value. Nevertheless, the whole evolution process from normal cycling to abnormal cycling, and eventually to thermal runaway is still well captured by the present model.

Fig. 9 displays the temperature variation with time of the cell surface from top view and the vertical section through the positive electrode tab from front view. These plots provide valuable insight of the underlying temperature changes from normal electric behaviour to thermal runaway. In contrast to Fig. 9(a)-(e), (f) shows about 100 K in temperature gradient of the whole cell, while Fig. 9(e) shows 1.05 K and Fig. 9(a)-(d) show only approximate 0.05 K. Fig. 9(a)-(c) depicts the 1st discharge, 1st charge and 6th charge process of the cell, respectively. A slight higher temperature was found in the two electrode aluminium tabs than in the main part of the cell. This is ascribed to the higher current density in the tab than in the main part of the cell, which results in higher temperature in the area close to the tabs than further away. However, once the cell goes into abnormal cycling process, the heat generation within the cell is dominated by the thermal reactions instead of the electric behaviour, and the self-heating rate of the cell
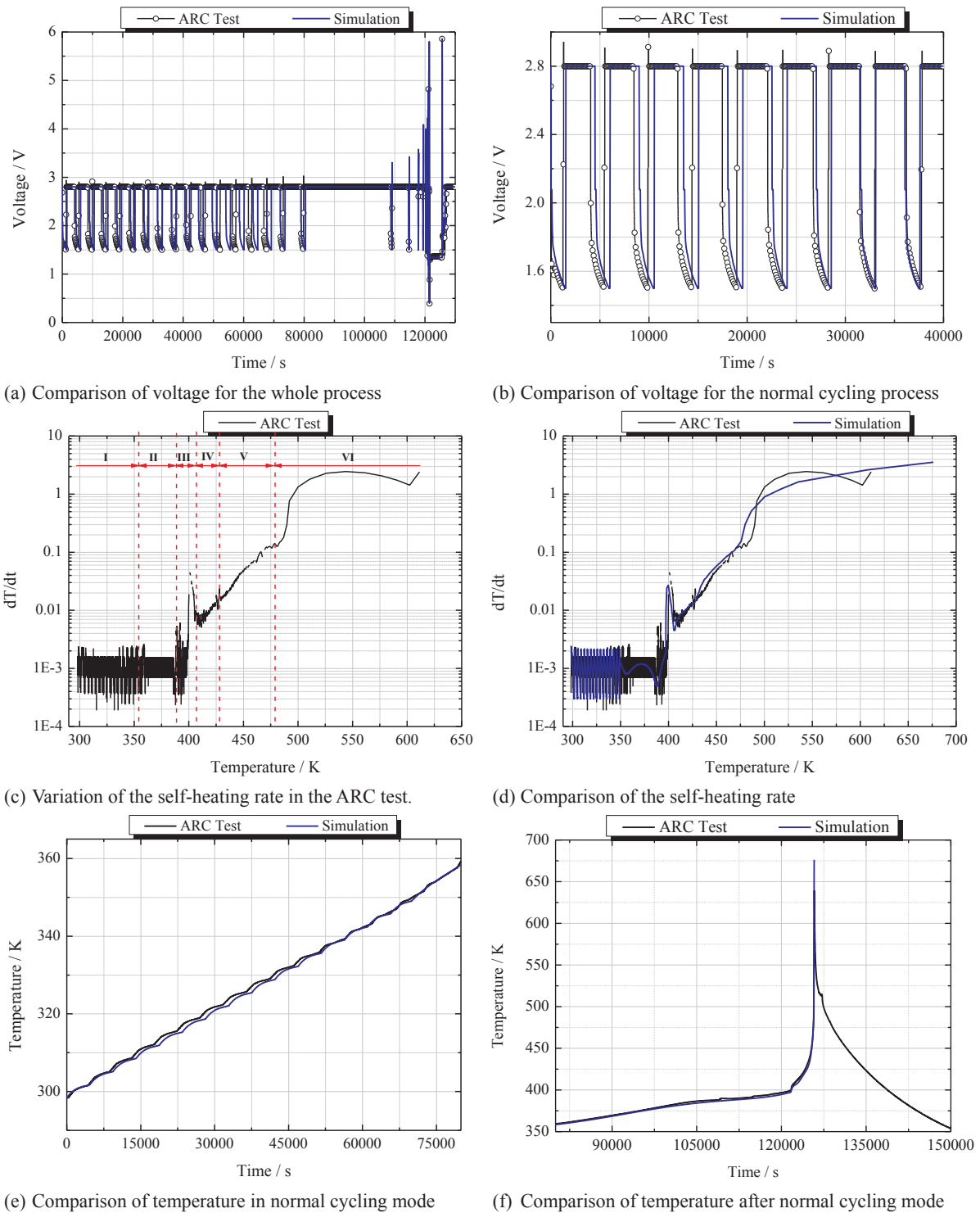
(a) Comparison of voltage for the whole process

(b) Comparison of voltage for the normal cycling process

(c) Variation of the self-heating rate in the ARC test.

(d) Comparison of the self-heating rate

(e) Comparison of temperature in normal cycling mode

(f) Comparison of temperature after normal cycling mode

Fig. 8. Comparisons of predicted and ARC test results on the cell at the current rate of 1.5 C under adiabatic condition.

increases with time. As a consequence, higher temperature was found in the core rather than in the tabs or edge of the cell as shown in Fig. 9(d)-(f). When the self-heating rate is not very high, the heat generated within the cell is transferred to the surface of the cell in a relatively short time. Thus, the temperature gradient of the cell is not evident as shown in Fig. 9(d) and (e). While owing to the sharp increase in self-heating rate as shown in Fig. 8(c) during stage VI, Fig. 9(f) shows much higher temperature gradient. Therefore, although the temperature within the cell centre is as high as 675 K, the surface of the cell may still show a lower temperature as 615 K. The above comparison

demonstrates that the model can predict the electrical and thermal performance of the cell with reasonably good accuracy.

5. Case study

5.1. High rate behaviour under adiabatic condition

The model is now applied to predict the electro-thermal performance for high rate condition which has not been covered in the ARC tests. Fig. 10 shows the predicted effect of changing the current rate to
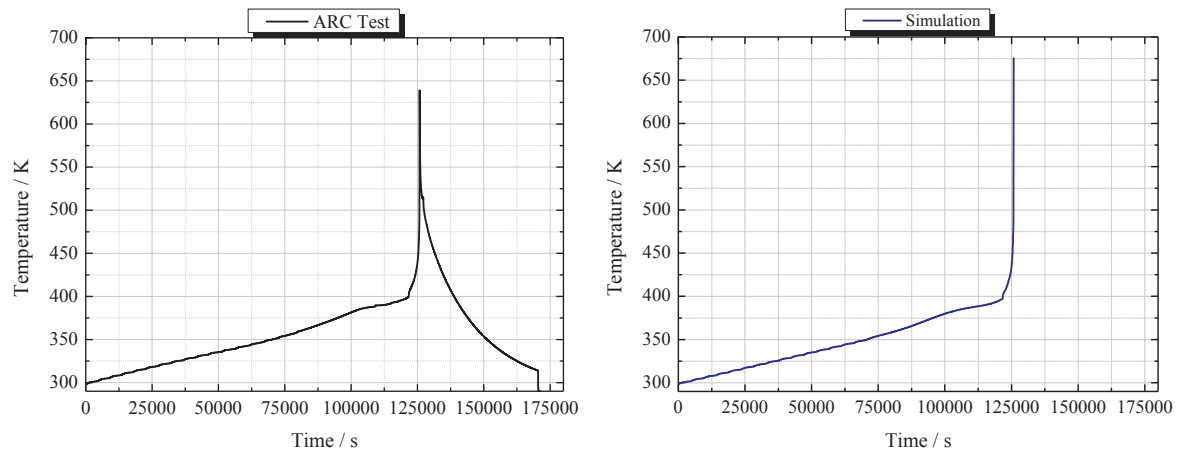
(g) Temperature variation obtained from ARC test during the whole process

(h) Prediced temperature variation during the whole process
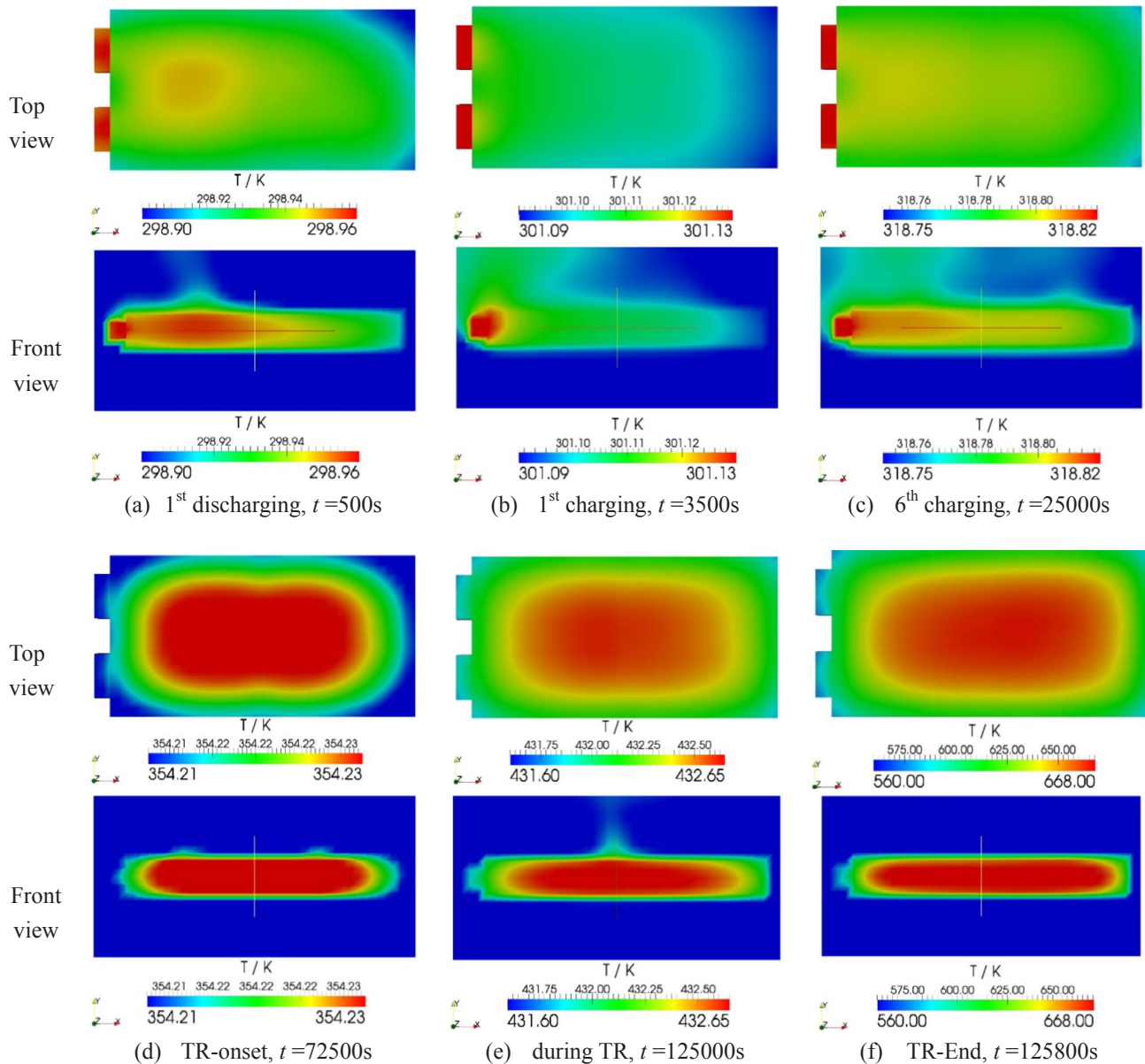
Fig. 8. (*continued*)

(a) 1st discharging, t =500s   (b) 1st charging, t =3500s   (c) 6th charging, t =25000s

(d) TR-onset, t =72500s   (e) during TR, t =125000s   (f) TR-End, t =125800s

Fig. 9. Temperature variation with time on the cell surface from top view, and the vertical section through the positive electrode tab from front view.

(a) Electrical and thermal behavior of the cell under 3C

(b) Electrical and thermal behavior of the cell under 5C

(c) Temperature of the cell under 1.5, 3 or 5C

(d) Temperature of the cell under 1.5, 3 or 5C for the whole process contained TR
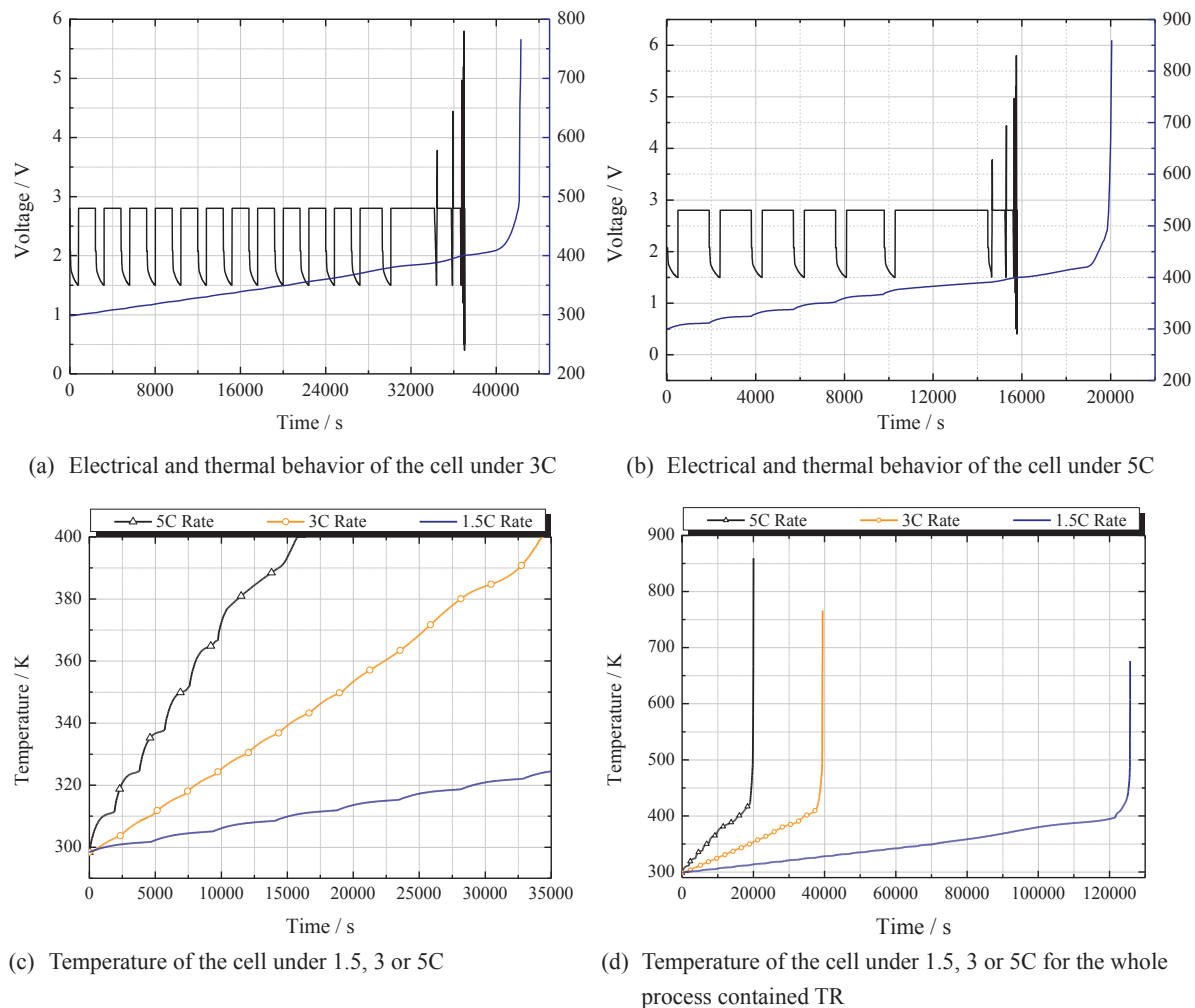
Fig. 10. Predictions for different discharging rates of 1.5 C, 3 C and 5 C.

3 C and 5 C. As shown in Fig. 10(a) and (b), when the temperatures increase to about 370 K and 376 K for the cells cycled under 3 C and 5 C, respectively, the two cells enter abnormal charging processes with longer time than previous normal charging processes. For the 13th cycle in 3 C case and the 6th cycle in the 5 C case, the cells still present a normal discharge process but an abnormal charging process with longer duration. Subsequently, the cells show abnormal cycling behaviour and significant loss of function at about 400 K. Meanwhile, the temperature of the cell increases evidently from 400 K, reaching the peak in the following 5000 s. There are similarities as well as differences in the cases of 5 C, 3 C and 1.5 C. As shown in Fig. 10(c), the cells cycled at 3 C and 5 C rate also exhibit periodic increases in the temperature, but the rate of the increase is faster for higher current rate and not directly proportional to the current rate. As described in Eq. (7), with the increase of the current, the heat generation also increases. In addition, the heat generation is proportional to both the current rate and its square [33]. As such, the cells cycled at higher rate enter abnormal process in much shorter time than that cycled at lower rate. Furthermore, the higher temperature rise rate is not only related to the increased electrical heat but also the thermal reaction heat. Fig. 10(d) shows that the temperature rises faster during the initial stage of the thermal reactions. Accordingly as seen from Eq. (13), the reaction heat is also higher. Consequently, the maximum temperature reached by the cell cycled under 3 C and 5 C rate is 766 K and 860 K, which are 91 K and 185 K higher than the peak temperature predicted for the cell cycled under 1.5 C.

Fig. 11 shows the temperature contour of the cell cycled at 3 C rate under adiabatic condition from top and front views. Fig. 11(a)-(c) are the temperature distribution of the cell and the surroundings during normal cycling process. Fig. 11(d) shows similar images of temperature distribution as in Fig. 11(a)-(c), demonstrating that heat transfer from the tabs to the cell body can also be found in Fig. 11(d) like the heat transfer observed in Fig. 11(a)-(c). In comparison with Fig. 9(d), it can be seen that although the temperature ranges of the cell in Figs. 9(d) and 11(d) are close, the distribution of the cell in these two figures are clearly different. In Fig. 9(d), the heat generation within the cell is dominated by thermal reactions. While in Fig. 11(d), the heat generation within the cell is strongly influenced by the electric behaviour, resulting in the temperature of the two tabs being higher than that of the cell centre.

Fig. 11(e) and (f) shows the temperature of the cell and airflow when the cell is in the early and final stages of thermal runaway. The images shown in Fig. 11(e) show higher temperatures in the cell centre than the tabs, which are close to those shown in Fig. 9(d) and (e). However, the temperature difference is relatively small at 0.3 K. Hence it can be assumed that this is the start when the effect of thermal reaction heat is higher than that of the electric behaviour on the temperature of the cell. One can also find an approximate start process in Fig. 9(d). However, Fig. 11(e) and (d) are not consistent with the temperature range of the cell, the former is around 410 K and almost 56 K higher than the later. Therefore, the cell discharged at 3 C rate provides a greater temperature boost to the reactants in the cell than
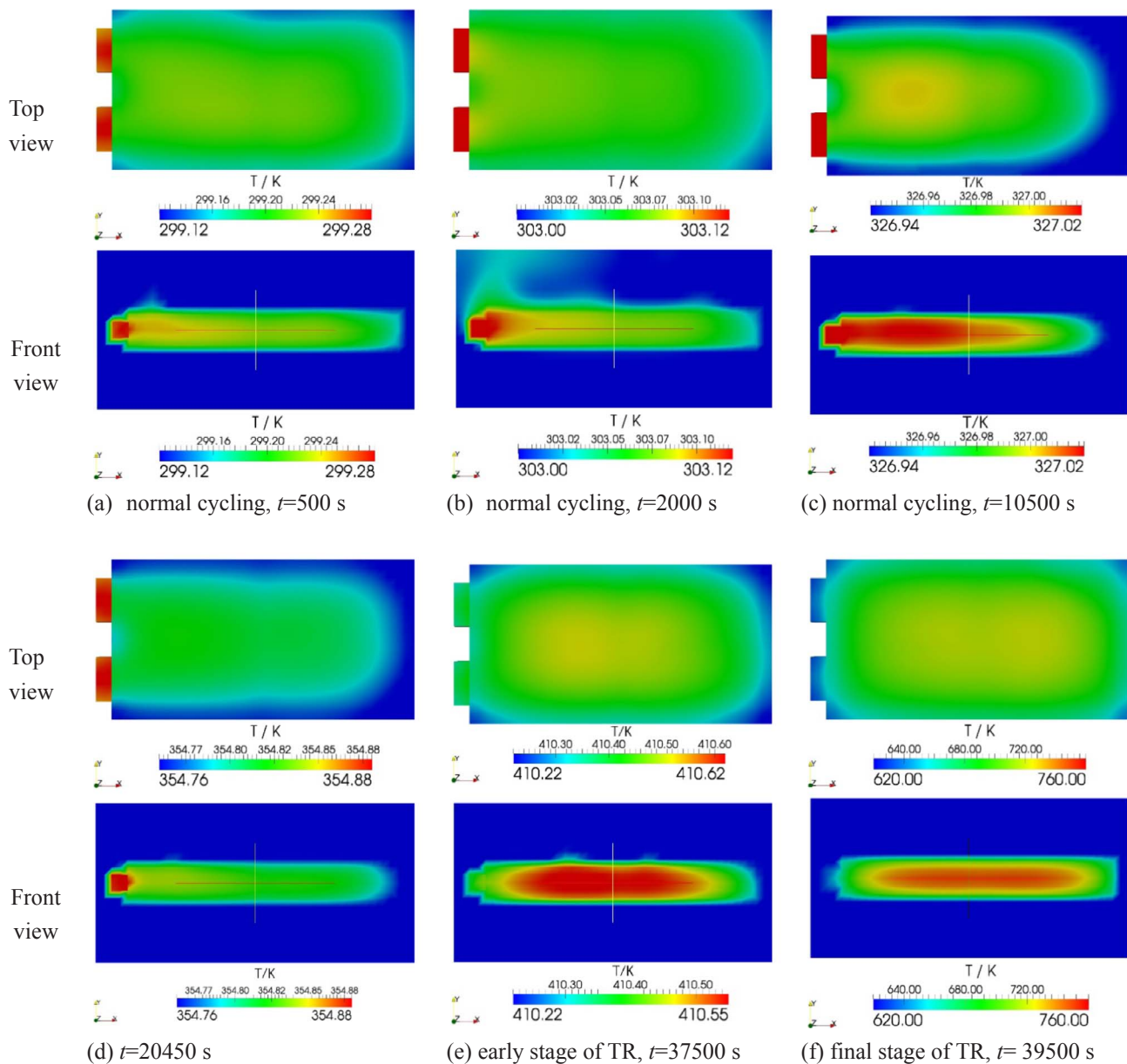
Fig. 11. Cell surface temperature variation with time from top view and the vertical section through the positive electrode tab from front view cycled at 3 C rate under adiabatic condition.

the 1.5 C cell. This also contributes to a higher peak temperature (around 760 K) found in Fig. 11(f). The temperature difference is about 140 K in Fig. 11(f), it is 40 K higher than the temperature difference shown in Fig. 9(f). The quick increase of the heat generation by the accelerated thermal reactions is responsible for the uneven temperature distributions here. These results demonstrate the model can be used to provide valuable insight about the heat transfer progress in the cell and the development of the thermal runaway. The cell under 5 C rate shows similar behaviour as the one under 3 C, with a faster increment on temperature and higher peak temperature. As such the detailed temperature contour within the cell is not repeated here.
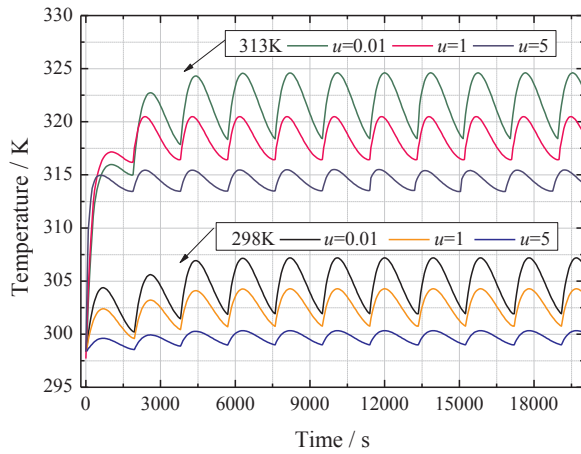
5.2. Air cooling under surrounding temperatures of 298 K and 313 K

To study the effect of air cooling on the performance of the cell, three airflow velocities of 0.01, 1.0 and 5.0 m s^{-1} are applied at the cell surfaces. The air is blown horizontally with the inlet on the left side of the electrode tabs and the outlet on the right side of the cell. The

distance from the top of airflow to the top surface of the cell is 16 mm, which is also the thickness of the airflow channel.

Fig. 12 shows the cell temperature variations under 5 C (Fig. 12a), 3 C (Fig. 12b) and 1.5 C (Fig. 12c) when subjected to various airflows under surrounding temperatures of 298 K and 313 K. After one or two cycles, the cells reach steady-state and show periodical change in the temperature. From the temperature rise rate of the first and second cycles, it can be seen that higher velocities of the airflow shorten the time for the cells to achieve steady-state no matter how the current rate is. In the steady-state situation, the cells show temperature rise during discharge process and decrease in charge process. This is consistent with Eq. (7), in which the reversible heat is negative when the cell is charging. Thus the electrical heat in charge process is less than that in discharge process. Under the cooling effect of airflow, the temperature decreases when the heat dissipation is larger than heat generation.
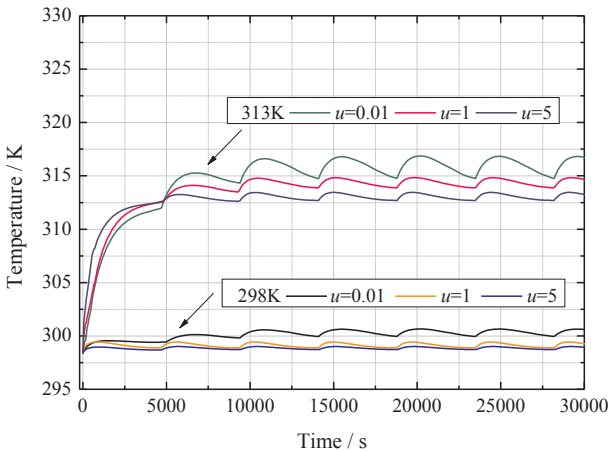
A comparison with the three figures in Fig. 12 indicates that the temperature variation during one cycle increases with the increase of the current rates. In airflow of 0.01 m s^{-1}, for one cycle during the

(a) Temperature variations of cells under 5C

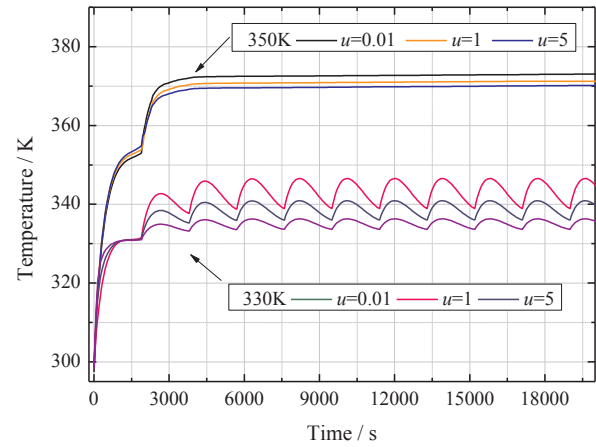(a) Temperature variations of cells under 5C
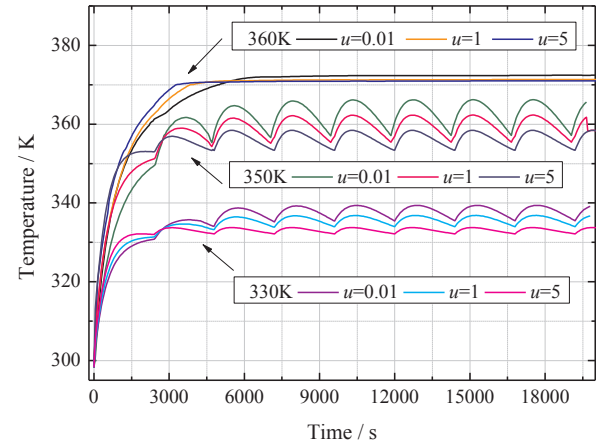

(b) Temperature variations of cells under 3C
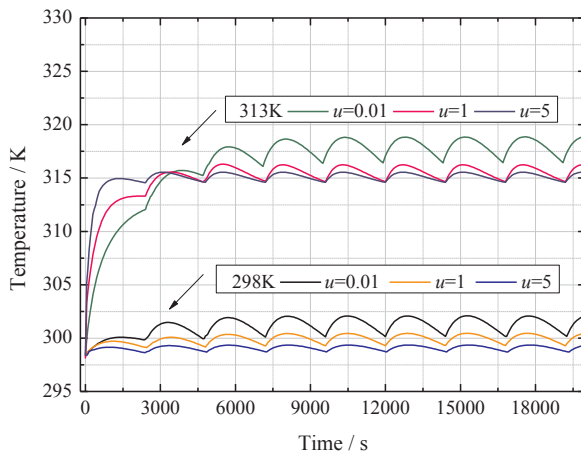
(b) Temperature variations of cells under 3C

(c) Temperature variations of cells under 1.5C

(c) Temperature variations of cells under 1.5C

Fig. 12. Cell temperature variations when subjected to air cooling at 0.01, 1 and 5 m s^{-1} under surrounding temperatures of 298 and 313 K.
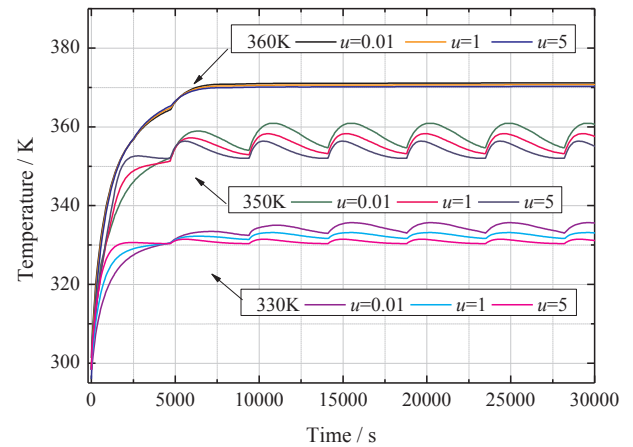
Fig. 13. Cell temperature variations when subjected to airflows of 0.01, 1 and 5 m s^{-1} under surrounding temperatures of 330 K, 350 K or 360 K.

steady-state situation, the current rates of 5, 3 and 1.5 C result in maximum temperature rises of 5.2, 1.9 and 0.7 K at 298 K and 6.2, 2.4, 1.5 K at 313 K. This indicates that cells cycled under high rate need to be cooled down to prevent excessive temperature rise.

By increasing the velocity of airflow to 1 and 5 m s^{-1}, the temperature variation during one cycle decreases. With the cooling effect of 5 m s^{-1} airflow, approximate temperature ranges are obtained for cells

under different current rates. The differences among them are less than 1.3 K and 1.9 K, for cells under ambient temperatures of 298 K and 313 K, respectively. Cells under 5 C rate show a temperature decrease of about 4 K on the maximum temperature rise when subjected to airflows with 5 m s^{-1}. This implies that the cooling effect of the airflow on the cell is improved by the increased velocity under these temperature conditions.

5.3. Air cooling conditions under elevated temperature conditions

Fig. 13 shows the cell temperature variations at various current rates under elevated surrounding temperatures of 330 K, 350 K and 360 K. When the temperature is 330 K, cells show normal cycling behaviour. Like the cells shown in Fig. 12, these cells also reached steady-state after the first or the second cycle. Comparing cells at different temperatures, it can be seen that the temperature variation during each cycle increases with the increase of the surrounding temperature. For instance, in 0.01 m s^{-1} airflows, the maximum temperature increase during each cycle for cells under 5 C rate at 330 K is 7.7 K, which is 1.5 K and 2.5 K higher than the cells at 313 and 298 K, respectively. For cells under 3 C and 1.5 C rates, same change tendency in temperature can be found. There are two major differences for cells under different current rates. One is the temperature range of the cell, which is higher under higher current rates. The other difference is the tolerance of high temperature. As shown in Fig. 13a, when the ambient temperature is 350 K, the temperature of the cell is over than 370 K during the second cycle. The higher current under 5 C induces larger polarization and resistance of the cell. The SEI decompositions occurred around this temperature also increases the resistance of the cell and decreases the lithium ions diffusion rate. The electro-thermal coupled effect results in the abnormal cycling behaviour. As in these considered cases, the heat generated is balance by the heat dissipated, the cell temperature stays almost constant, slightly higher than 370 K. Because of less heat generation at lower current rates, the cells under 3 and 1.5 C can still cycle in a temperature range lower than 370 K, even at ambient temperature of 350 K. But when the ambient temperatures increase to 360 K, the temperature of the cell achieves to 370 K. Then the electro-thermal coupled effect also make the cycling behavior abnormal. Therefore, high current rate reduces the tolerance of high surrounding temperature of the cell.

Comparison between cells subjected to 1 and 5 m s^{-1} airflows is conducted to study the effect of airflow on cell behaviour. When the cells are in normal cycling situation, the increase in airflow velocities mitigates the temperature variations. However, this effect decreases with the increase of surrounding temperature and current rate. In contrast to Fig. 12, cells at 330 K in Fig. 13 still show larger temperature variations, especially when they are under 5 C rate. For the cell at 350 K under 5 C rate and the cells at 360 K under 3 C and 1.5 C rates, it can be seen that the increase in velocities make minor difference to the cell behaviour. The normal cycling still cannot be sustained for these cells, even with 5 m s^{-1} airflow. Nevertheless, the temperature in the steady-state is marginally lower when the cell subjected to airflow with higher velocity.

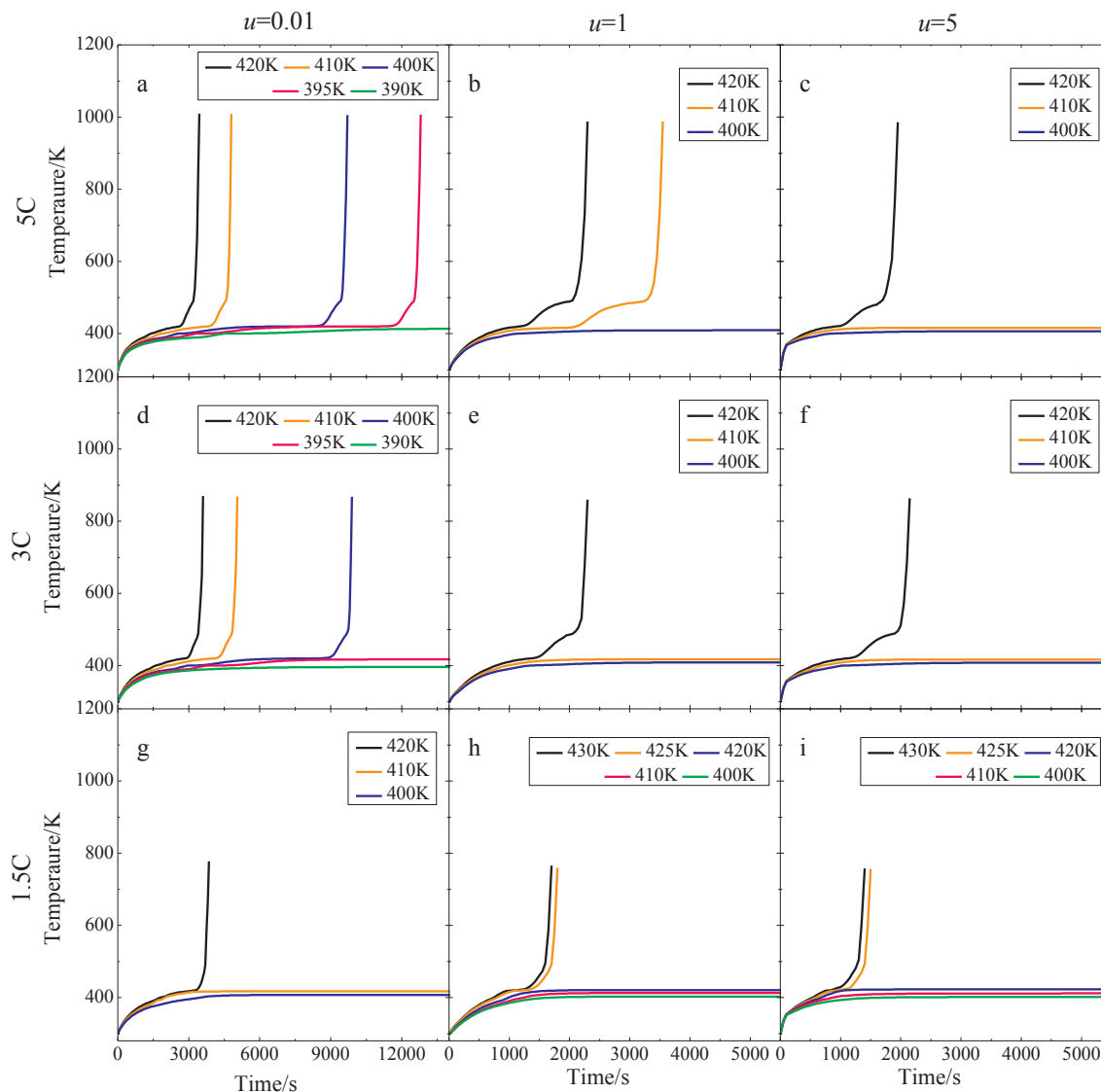Fig. 14 shows the cell temperature variations within much higher

Fig. 14. Cell temperature variations subjected to airflows of 0.01, 1 and 5 m s^{-1} within 390–430 K.

ambient temperature range of 390–430 K (127–157 °C) during cycling under 5 C (Fig. 14a-c), 3 C (Fig. 14d-f) and 1.5 C (Fig. 14g-i) rates. In practical situations, such high surrounding temperatures can be caused by overheating, cell failure or thermal runaway of a neighbouring cell. As shown in Fig. 14a, d and g for the 0.01 m s^{-1} airflow, thermal runaway occurred for the cells charged at 5, 3 and 1.5 C rates at 395 K, 400 K and 420 K. While it can be seen also in same figures, cycling at these rates under surrounding temperatures lower than these values did not lead to thermal runaway and the cells stayed in steady-state condition. Although the cells under such high surrounding temperatures cannot cycle normally under 5, 3 or 1.5 C rate, the transient discharge process during the initial stage still play a role in the cell behaviour. High current rate speeds up the initial temperature rise and activates the abuse thermal reactions in the cell earlier than low current rates. For instance, at 420 K, cells cycled at 5 C show thermal runaway 300 and 700 s earlier than cells cycled at 3 C and 1.5 C rates. Cells under 1.5 C do not even show thermal runaway at 410 K. The detailed time of thermal runaway occurrence under different conditions is summarized in Table 3.

When the velocity of the airflow increases to 1 to 5 m s^{-1}, as shown in Fig. 14b-c, e-f and h-i, thermal runway does not happen when the surrounding temperature is lower than 410 K. On the other hand, thermal runaway occurs when the ambient temperature is higher than 425 K and even when the cell was subjected to 5 m s^{-1} airflow and under low rate of 1.5 C. The airflow with higher velocity enhances cell cooling and helps it to stay in the steady-state and close to the surrounding temperature. Owing to the high velocity of airflow, the heat transfer with surroundings keeps the cell staying at 412 K when the ambient temperature is 410 K. Thus the thermal runaway observed in Fig. 14a and b does not appear in Fig. 14c. However, when the ambient temperature is higher than 425 K, thermal reactions during stage V analyzed in Section 4.2 would be easily activated. The positive electrode material decomposes and generates heat as well as oxygen. The solvent is oxidized, generating enormous heat and gas, which finally contribute to the thermal runaway. The predictions show that airflow of 1 or 5 m s^{-1} velocity is capable of enhancing the cell tolerance to high temperature. However, when the cell is at a critical stage, more efficient cooling technique is required to prevent occurrence of thermal runaway. The present model can be used to assist battery thermal management by monitoring cell temperatures so mitigation measurement can be used to prevent the cells from reaching the critical temperature of 425 K and trigger thermal runaway.

5.4. Effect of the airflow channel thickness

To enhance the energy density and keep the mechanical integrity of a battery pack, the cells in a pack are always arranged compactly to fit within confined spaces. This means that the spaces left for the cooling system is limited. To balance the need for high energy density and safety, adequate thickness of the airflow channel should be considered in designing thermal management systems. In the cases studied in the previous sections, the airflow channel is 16 mm thick, which is twice the thickness of the cell. Further parametric studies have been conducted to investigate the effect of varying the channel thickness. It has been found that the decrease of the airflow channel thickness to 4 mm and 2 mm can result in substantial cell temperature changes. Fig. 15 shows cell temperature variations when subjected to 0.01 m s^{-1} airflow with channel thickness of 4 mm. It is shown that although the cell at 360 K is still undergoing normal discharge under 5 C rate in the first discharge process, it cannot cycle continuously and maintain steady-state in the second cycle. Cell at 370 K shown in Fig. 15a cannot cycle normally and instead goes into thermal runaway. When the ambient temperature increases to 380 K, thermal runaway is observed. Cell at 390 K shows thermal runaway 3700 s earlier than the one at 380 K. When the velocity of the airflow increases to 1 and 5 m s^{-1}, the cells at 380 and 390 K ambient temperature still show thermal runaway as

shown in Fig. 15b.

Fig. 15(c) and (d) shows the temperature variation of cells in airflow with channel thickness of 2 mm. The cells undergo thermal runaway at the surrounding temperatures of 360 and 370 K. The cell at 350 K shows a steady-state with temperature at 380 K, which is 10 K higher than the cell shown in Fig. 13a. In contrast with cells in Fig. 14a, cells in Fig. 15a and c show a lower tolerance of high surrounding temperature. These parametric studies illustrate that the decrease of airflow channel thickness reduces the cell tolerance to high surrounding temperature; and when the airflow channel is too small, thermal runaway cannot be prevented by simply increasing airflow velocity. Thermal runaway happens to the cells in Fig. 15b earlier with the increase of airflow velocity, which are similar to the cells in Fig. 15d. The relatively low thermal conductivity and limited air flow is not sufficient to achieve sufficient dissipation of the heat generated by the cell when the airflow channel is too narrow. On the contrary, the combined effect of high surrounding temperature and limited airflow provides a certain degree of thermal insulation to hinder heat dissipation. Therefore, air cooling system with narrow channel might not be effective when the cell is in high surrounding temperature. For the cell studied in this work, thermal runaway would arise in about 6 h when the ambient temperature is 360 K (87 °C).

6. Conclusions

A 3D electro-thermal model has been developed within the frame of open source CFD code OpenFOAM by coupling electric conduction with heat transfer and energy balance for a single LIB cell. The model solves

Table 3
Critical parameters for the cells cycled at different current rates under different surrounding temperatures and airflow velocities.

Current rate	Surrounding temperature/K	Airflow velocity/ m s^{-1}	Status	Time to TR/s
1.5 C	≤ 350	0.01/1/5	NC[a]	–
	360	0.01/1/5	AC[b]	
	400	0.01/1/5	AC	–
	410	0.01/1/5	AC	–
	420	0.01	TR[c]	3600
		1/5	AC	–
	425	1	TR	1550
		5		1300
	430	1	TR	1450
		5		1150
3 C	≤ 350	0.01/1/5	NC	–
	360	0.01/1/5	AC	–
	390/395	0.01/1/5	AC	–
	400	0.01	TR	9300
		1/5	AC	–
	410	0.01	TR	4500
		1/5	AC	–
	420	0.01	TR	3200
		1		1700
		5		1450
5 C	< 350	0.01/1/5	NC	–
	350	0.01/1/5	AC	–
	390	0.01	AC	–
	395	0.01	TR	12100
	400	0.01	TR	9000
		1/5	AC	–
	410	0.01	TR	4250
		1		2400
		5	AC	–
	420	0.01	TR	2900
		1		1500
		5		1250

[a] NC: normal cycling.
[b] AC: abnormal cycling, steady state.
[c] TR: thermal runaway.

(a) 4mm thickness, u=0.01 m s^{-1}

(b) 4mm thickness, u=0.01, 1 and 5 m s^{-1}

(c) 2mm thickness, u=0.01 m s^{-1}
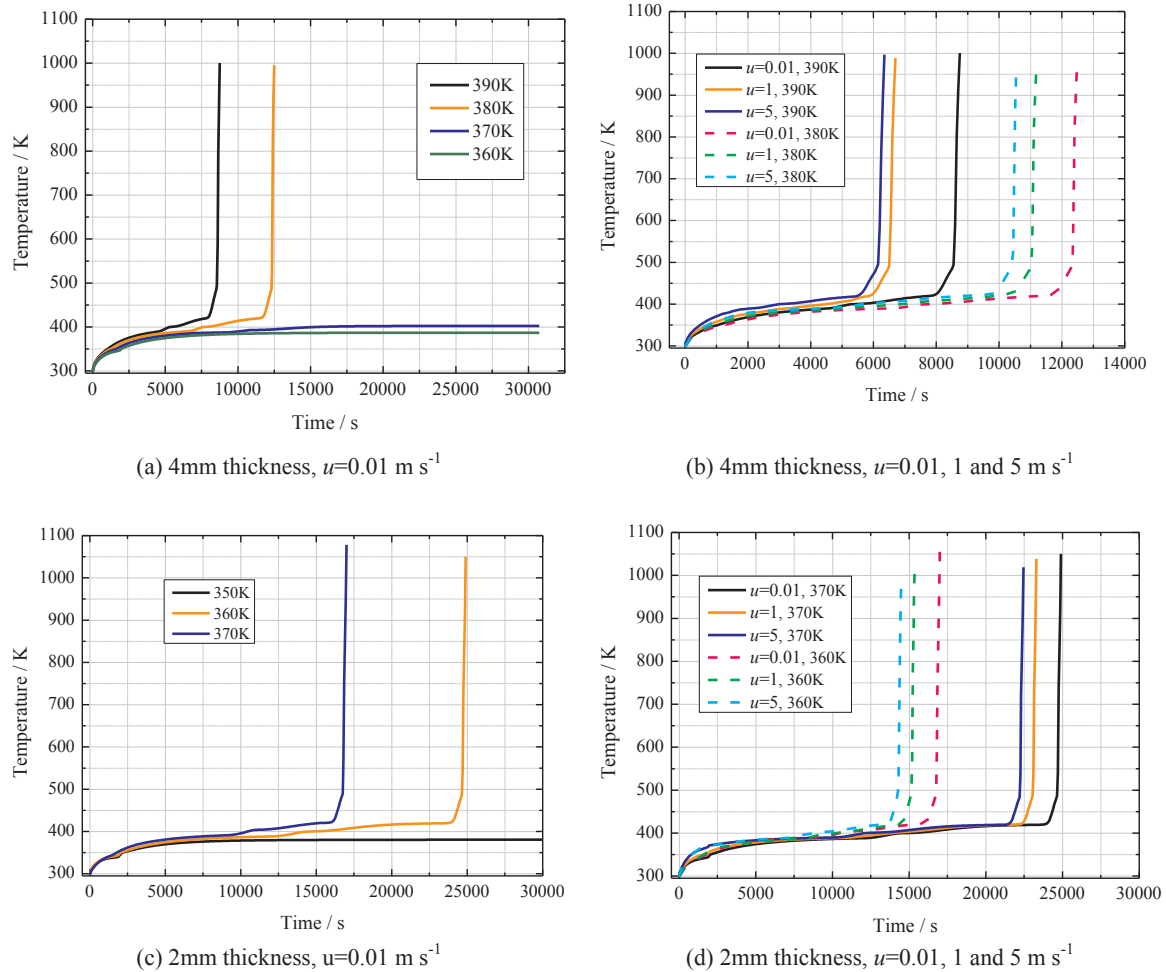
(d) 2mm thickness, u=0.01, 1 and 5 m s^{-1}

Fig. 15. Temperature variations of cells subjected to airflows within channels of different thickness.

a highly coupled system of equations that describe the relations between the electrical and thermal characteristics of the cell, as well as their interactions with the surroundings. The model has been validated with published and newly generated experimental data for the predictions of voltage, current and temperature variation within the cell under various conditions. Reasonably good agreement has been achieved between the predictions and measurements for all these parameters. In addition, the model has reproduced well the evolution process of a cell from normal to abnormal cycling until thermal runaway.

Subsequent parametric studies for LiNi$_{0.33}$Co$_{0.33}$Mn$_{0.33}$O$_2$/ Li$_{1.33}$Ti$_{1.67}$O$_4$ (LNCMO/LTO) cells have also been conducted using the validated model, covering normal cycling to abuse conditions and thermal runaway. The following specific conclusions may be drawn from the parametric studies for the numerically tested LIB cell:

(1) There is a low limit of surrounding temperature for transition to thermal runaway. When the temperature of the surroundings is higher than 425 K, thermal runaway can occur, even under low discharge rate like 1.5 C, or in airflow with high velocity like 5 m s^{-1}. Cell failure or thermal runaway can result in temperatures higher than 425 K and propagation of thermal runway to other cells.

(2) The model can be used to determine critical temperatures under different air cooling conditions and current rates; and aid the design of BMS to prevent thermal runaway propagation.

(3) For cells subjected to air cooling, the thickness of the airflow channel is a critical factor to achieve desirable cooling effect. Under the same discharging of 5 C and passive airflow cooling, the cells enter thermal runaway when the ambient temperatures are higher than 360 K, 380 K and 395 K if the thickness of the airflow channel is 2, 4 and 16 mm, respectively.
It is hence essential to provide sufficient airflow channel thickness in battery pack design when air cooling system is adopted.

(4) When the heat generated within the cell cannot be transferred to the surroundings, which is adiabatic condition, higher discharge rate can clearly lead to faster development of abnormal conditions and earlier thermal runaway. However, the higher rate do not show such substantial effect when airflow is introduced to the surroundings with temperature less than 370 K. Airflow with 5 m s^{-1} velocity can reduce the temperature difference between the cells discharged at different rates. The present model can be used to estimate the airflow velocity required for effective cooling.

(5) Airflow at high velocities can shorten the time for the cell to reach steady-state and prevent over-heating and hence thermal runaway when the surrounding temperature is lower than 395 K. Above this temperature, air cooling was found to be insufficient to prevent thermal runaway and more efficient cooling technique should be introduced.

In summary, the present study has resulted in a valid electro-thermal model and demonstrated its capability to predict the electrical and thermal performance of LIB cells from normal operating to abuse conditions and thermal runaway, under different discharging current rates and environmental conditions. Given that the physics and structure of the model had been developed for generic environmental

conditions and configurations, it can be easily extended to other LIBs and LIB modules with different combinations of materials, geometries, operating conditions and cooling effects. The model can potentially be used to assist BMS from the safety perspective.

Acknowledgments

References

[1] Golubkov AW, Scheikl S, Planteu R, Voitic G, Wiltsche H, Stangl C, et al. Thermal runaway of commercial 18650 Li-ion batteries with LFP and NCA cathodes – impact of state of charge and overcharge. RSC Adv 2015;5:57171–86.

[2] Escobar-Hernandez HU, Gustafson RM, Papadaki MI, Sachdeva S, Mannan S. Thermal runaway in lithium-ion batteries: incidents, kinetics of the runaway and assessment of factors affecting its initiation. J Electrochem Soc 2016;163:A2691–701.

[3] Feng X, He X, Ouyang M, Lu L, Wu P, Kulp C, et al. Thermal runaway propagation model for designing a safer battery pack with 25 Ah LiNixCoyMnzO2 large format lithium ion battery. Appl Energy 2015;154:74–91.

[4] Bandhauer TM, Garimella S, Fuller TF. A critical review of thermal issues in lithium-ion batteries. J Electrochem Soc 2011;158:R1.

[5] Lu L, Han X, Li J, Hua J, Ouyang M. A review on the key issues for lithium-ion battery management in electric vehicles. J Power Sources 2013;226:272–88.

[6] Kim GH, Pesaran A, Spotnitz R. A three-dimensional thermal abuse model for lithium-ion cells. J Power Sources 2007;170:476–89.

[7] Abada S, Marlair G, Lecocq A, Petit M, Sauvant-Moynot V, Huet F. Safety focused modeling of lithium-ion batteries: a review. J Power Sources 2016;306:178–92.

[8] Ye Y, Shi Y, Cai N, Lee J, He X. Electro-thermal modeling and experimental validation for lithium ion battery. J Power Sources 2012;199:227–38.

[9] Saw LH, Ye Y, Tay AAO. Electrochemical–thermal analysis of 18650 lithium iron phosphate cell. Energy Convers Manage 2013;75:162–74.

[10] Liu R, Chen J, Xun J, Jiao K, Du Q. Numerical investigation of thermal behaviors in lithium-ion battery stack discharge. Appl Energy 2014;132:288–97.

[11] Khan MR, Kaer SK. Three dimensional thermal modeling of Li-ion battery pack based on multiphysics and calorimetric measurement. In: 2016 IEEE vehicle power and propulsion conference (VPPC); 2016. p. 1–6.

[12] Marzband M, Sumper A, Ruiz-álvarez A, et al. Experimental evaluation of a real time energy management system for stand-alone microgrids in day-ahead markets. Appl Energy 2013;106:365–76.

[13] Jiang J, Ruan H, Sun B, Zhang W, Gao W, Wang LY, et al. A reduced low-temperature electro-thermal coupled model for lithium-ion batteries. Appl Energy 2016;177:804–16.

[14] Hatchard TD, Macneil DD, Basu A, Dahn JR. Thermal model of cylindrical and prismatic lithium-ion cells. J Electrochem Soc 2001;148:A755–61.

[15] Guo G, Long B, Cheng B, Zhou S, Xu P, Cao B. Three-dimensional thermal finite element modeling of lithium-ion battery in thermal abuse application. J Power Sources 2010;195:2393–8.

[16] Lopez CF, Jeevarajan JA, Mukherjee PP. Characterization of lithium-ion battery thermal abuse behavior using experimental and computational analysis. J Electrochem Soc 2015;162:A2163–73.

[17] Spotnitz R, Franklin J. Abuse behavior of high-power, lithium-ion cells. J Power Sources 2003;113:81–100.

[18] Lee CH, Bae JS, Jang M. A study on effect of lithium ion battery design variables upon features of thermal-runaway using mathematical model and simulation. J Power Sources 2015;293:498–510.

[19] Liang G, Zhang Y, Han Q, Liu Z, Jiang Z, Tian S. A novel 3D-layered electro-chemical-thermal coupled model strategy for the nail-penetration process simulation. J Power Sources 2017;342:836–45.

[20] Melcher A, Ziebert C, Rohde M, Seifertet HJ. Modeling and simulation the thermal runaway behavior of cylindrical li-ion cells-computing of critical parameter. Energies 2016;9:292.

[21] http://www.teslarati.com/tesla-short-circuit-cause-for-model-s-norway-fire/.

[22] Sun Q, Wang Q, Zhao X, Sun J, Lin Z. Numerical study on lithium titanate battery thermal response under adiabatic condition. Energy Convers Manage 2015;92:184–93.

[23] Jeon DH, Baek SM. Thermal modeling of cylindrical lithium ion battery during discharge cycle. Energy Convers Manage 2011;52:2973–81.

[24] Stewart S, Albertus P, Srinivasan V, Plitz I, Pereira N, Amatucci G, et al. Optimizing the performance of lithium titanate spinel paired with activated carbon or iron phosphate. J Electrochem Soc 2008;155:A253–61.

[25] Kwon KH, Shin CB, Kang TH, Kim CS. A two-dimensional modeling of a lithium-polymer battery. J Power Sources 2006;163:151–7.

[26] Tiedemann Newman. Potential and current distribution in electrochemical-cells - interpretation of the half-cell voltage measurements as a function of reference-electrode location. J Electrochem Soc 1993;140:1961–8.

[27] Gu H. Mathematical analysis of a Zn/NiOOH cell. J Electrochem Soc 1983;130:1459–64.

[28] Chacko S, Chung YM. Thermal modelling of Li-ion polymer battery for electric vehicle drive cycles. J Power Sources 2012;213:296–303.

[29] Bernardi D, Pawlikowski E, Newman J. A general energy balance for battery systems. J Electrochem Soc 1985;132:5–12.

[30] Wang Q, Ping P, Zhao X, Chu G, Sun J, Chen C. Thermal runaway caused fire and explosion of lithium ion battery. J Power Sources 2012;43:210–24.

[31] Kong DP, Ping P, Wang QS, Sun JH. Study on high temperature stability of LiNi0.33Co0.33Mn0.33O2 /Li4Ti5O12 Cells from the safety perspective. J Electrochem Soc 2016;163:A1697–704.

[32] MacNeil D, Dahn J. Test of reaction kinetics using both differential scanning and accelerating rate calorimetries as applied to the reaction of LixCoO2 in non-aqueous electrolyte. J Phys Chem A 2001;105:4430–9.

[33] Zhu C, Li X, Song L, Xiang L. Development of a theoretically based thermal model for lithium ion battery pack. J Power Sources 2013;223:155–64.